

10

Integral Equation Methods for Three-Dimensional Bodies

While formulations for the interaction of electromagnetic fields with three-dimensional bodies are generally similar to the two-dimensional approaches of previous chapters, there are several differences. Obvious differences are that the zero-order Hankel function used as a two-dimensional Green's function is replaced by the three-dimensional Green's function $e^{-jkr}/4\pi r$ and the dimensionality of the integrals increases. Other differences that impact the implementation of these methods include the proportionally larger amount of data required to describe a three-dimensional scatterer model and the rapid growth of the number of unknowns with three-dimensional scatterer size. Three-dimensional scatterer models are also more difficult to generate and visualize than their two-dimensional counterparts. Finally, and perhaps most significantly, three-dimensional problems are inherently vector in nature.

This chapter begins by considering EFIE formulations applied to flat conducting plates and objects of arbitrary shape. Approaches using rectangular-cell models and triangular-cell models are used to illustrate vector basis functions of the CN/LT and LN/QT variety (Chapter 9). The triangular-cell EFIE formulation is extended to a combined-field (CFIE) formulation for closed conducting bodies in Sections 10.4 and 10.5 and to general homogeneous dielectric objects in Section 10.7. Section 10.6 considers the treatment of electrically small scatterers, where a conventional EFIE fails. Section 10.8 summarizes an approach for treating wires and wire-grid models, while Section 10.9 considers planar periodic structures. The analysis of microstrip antennas and scatterers requires a different Green's function to account for the substrate material (Section 10.10). Finally, Section 10.11 summarizes several volume integral formulations for three-dimensional heterogeneous scatterers.

10.1 SCATTERING FROM FLAT PERFECTLY CONDUCTING PLATES: EFIE DISCRETIZED WITH CN/LT ROOFTOP BASIS FUNCTIONS DEFINED ON RECTANGULAR CELLS

Consider one or more infinitesimally thin flat conducting plates located in the $z = 0$ plane and illuminated by an electromagnetic wave. The perfectly conducting material may be replaced by equivalent electric currents radiating in free space, where the equivalent currents represent the superposition of the current densities on both sides of the plate. In anticipation of a rectangular-cell model, components J_x and J_y are selected as the primary unknowns to be determined. The EFIE can also be separated into \hat{x} and \hat{y} components to produce the coupled equations

$$E_x^{\text{inc}}(x, y) = -\hat{x} \cdot \frac{\nabla \nabla \cdot + k^2}{j\omega\epsilon_0} \bar{A} \quad (10.1)$$

$$E_y^{\text{inc}}(x, y) = -\hat{y} \cdot \frac{\nabla \nabla \cdot + k^2}{j\omega\epsilon_0} \bar{A} \quad (10.2)$$

where the magnetic vector potential is

$$\bar{A}(x, y) = \iint [\hat{x} J_x(x', y') + \hat{y} J_y(x', y')] \frac{e^{-jkR}}{4\pi R} dx' dy' \quad (10.3)$$

and

$$R = \sqrt{(x - x')^2 + (y - y')^2} \quad (10.4)$$

Equations (10.1) and (10.2) are only valid on the location of the original plate(s).

Initially, we restrict the plate size and shape to a geometry that can be represented by equal-size rectangular cells, as illustrated in Figure 10.1, and approximate the current density with a superposition of the CN/LT “rooftop” basis functions defined in Section 9.13 and illustrated in Figure 10.2. Each rooftop function spans two adjacent cells on the plate and is centered at the edge between the two cells (Figure 10.3). Rooftop basis functions for the \hat{x} -component of the current density vary linearly in the x direction and

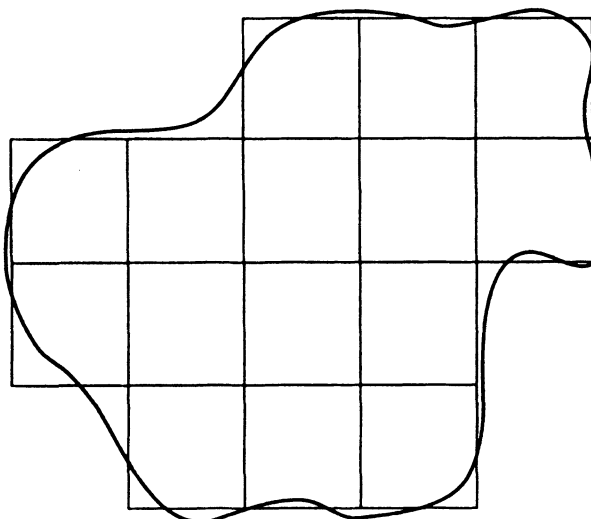


Figure 10.1 Rectangular-cell representation of an arbitrarily shaped plate.

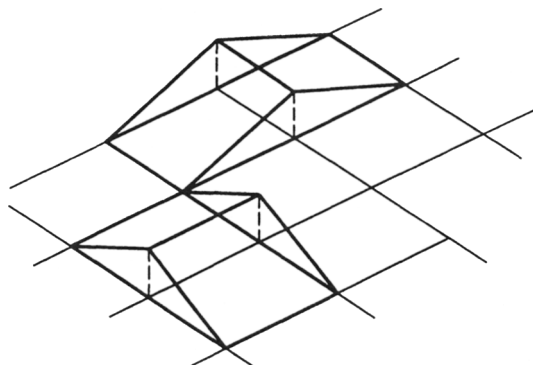


Figure 10.2 The CN/LT rooftop basis function defined on a rectangular cell.

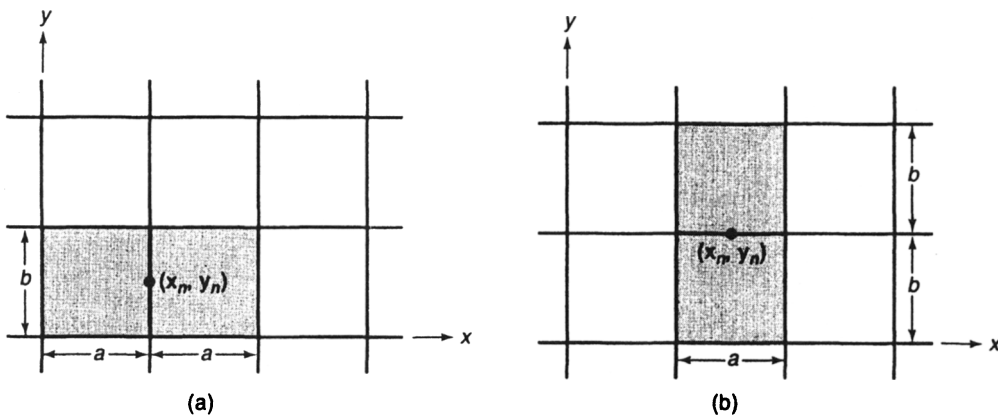


Figure 10.3 Location of rooftop basis functions within the rectangular-cell mesh.

are piecewise constant in the y direction, and vice versa. Using the fundamental triangle and pulse functions (Figure 5.1) and assuming that all cells in the model have dimensions $a \times b$, the rooftop functions can be written as

$$B_{xn}(x, y) = t(x; x_n - a, x_n, x_n + a)p(y; y_n - \frac{1}{2}b, y_n + \frac{1}{2}b) \quad (10.5)$$

$$B_{yn}(x, y) = t(y; y_n - b, y_n, y_n + b)p(x; x_n - \frac{1}{2}a, x_n + \frac{1}{2}a) \quad (10.6)$$

where (x_n, y_n) denotes the center of edge n . Using these basis functions, the current density is represented as

$$J_x(x, y) \cong \sum_{n=1}^M j_{xn} B_{xn}(x, y) \quad (10.7)$$

$$J_y(x, y) \cong \sum_{n=M+1}^N j_{yn} B_{yn}(x, y) \quad (10.8)$$

where the plate model consists of M interior cell edges associated with the \hat{x} -component of the current and $N - M$ interior cell edges associated with J_y . No basis functions are assigned to cell edges along the plate boundary, since the superimposed currents must vanish at the boundary.

In order to enforce the EFIE, we employ the “razor blade” testing functions depicted in Figure 10.4, which are defined as

$$T_{xm} = p(x; x_m - \frac{1}{2}a, x_m + \frac{1}{2}a) \delta(y - y_m) \quad (10.9)$$

$$T_{ym} = p(y; y_m - \frac{1}{2}b, y_m + \frac{1}{2}b) \delta(x - x_m) \quad (10.10)$$

and are spatially centered at the same location as the basis functions. The \hat{x} and \hat{y} components of the integral equation are tested with $T_x(x, y)$ and $T_y(x, y)$, respectively, in order to provide an additional degree of differentiability in directions where it is needed to absorb the derivatives in (10.1) and (10.2). This combination of basis and testing functions was suggested by Glisson and Wilton [1]. The testing process produces the $N \times N$ discrete system

$$\begin{bmatrix} \mathbf{A} & \mathbf{B} \\ \mathbf{C} & \mathbf{D} \end{bmatrix} \begin{bmatrix} \mathbf{j}_x \\ \mathbf{j}_y \end{bmatrix} = \begin{bmatrix} \mathbf{e}_x \\ \mathbf{e}_y \end{bmatrix} \quad (10.11)$$

Because the testing functions are even functions about $(x - x_m, y - y_m)$, the entries of the matrix can be expressed in convolution notation (Chapters 1 and 5) as

$$A_{mn} = \frac{-1}{j\omega\epsilon_0} T_{xm} * \left(\frac{\partial^2}{\partial x^2} + k^2 \right) (B_{xn} * G) \quad (10.12)$$

$$B_{mn} = \frac{-1}{j\omega\epsilon_0} T_{xm} * \left(\frac{\partial^2}{\partial x \partial y} \right) (B_{yn} * G) \quad (10.13)$$

$$C_{mn} = \frac{-1}{j\omega\epsilon_0} T_{ym} * \left(\frac{\partial^2}{\partial y \partial x} \right) (B_{xn} * G) \quad (10.14)$$

$$D_{mn} = \frac{-1}{j\omega\epsilon_0} T_{ym} * \left(\frac{\partial^2}{\partial y^2} + k^2 \right) (B_{yn} * G) \quad (10.15)$$

where the asterisk denotes two-dimensional convolution

$$U * V = \iint U(x', y') V(x - x', y - y') dx' dy' \quad (10.16)$$

The operations on the right-hand sides of (10.12)–(10.15) produce functions of x and y that are to be evaluated at $x = 0$ and $y = 0$. The Green's function appearing in these expressions is

$$G(x, y) = \frac{e^{-jk\sqrt{x^2+y^2}}}{4\pi\sqrt{x^2+y^2}} \quad (10.17)$$

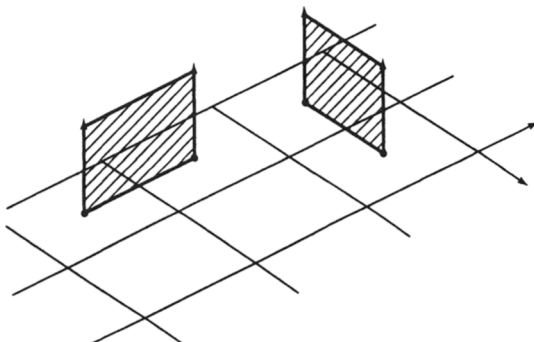


Figure 10.4 Razor-blade testing functions.

The right-hand side of the matrix equation contains entries

$$e_{xm} = \int_{x_m - a/2}^{x_m + a/2} E_x^{\text{inc}}(x, y_m, 0) dx \quad (10.18)$$

$$e_{ym} = \int_{y_m - b/2}^{y_m + b/2} E_y^{\text{inc}}(x_m, y, 0) dy \quad (10.19)$$

Because the geometry under consideration only involves basis and testing functions oriented along the x - or y -axis in the $z = 0$ plane, properties of the convolution operator can be exploited to enhance the efficiency of the impedance matrix calculations and reduce the number of required integrations. Specifically, since differentiation and convolution operators commute, Equations (10.12)–(10.15) are equivalent to

$$A_{mn} = \frac{-1}{j\omega\epsilon_0} \left[\left(\frac{\partial^2}{\partial x^2} + k^2 \right) (T_{xm} * B_{xn}) \right] * G \quad (10.20)$$

$$B_{mn} = \frac{-1}{j\omega\epsilon_0} \left[\frac{\partial^2}{\partial x \partial y} (T_{xm} * B_{yn}) \right] * G \quad (10.21)$$

$$C_{mn} = \frac{-1}{j\omega\epsilon_0} \left[\frac{\partial^2}{\partial x \partial y} (T_{ym} * B_{xn}) \right] * G \quad (10.22)$$

$$D_{mn} = \frac{-1}{j\omega\epsilon_0} \left[\left(\frac{\partial^2}{\partial y^2} + k^2 \right) (T_{ym} * B_{yn}) \right] * G \quad (10.23)$$

where the functions are evaluated at $x = 0$ and $y = 0$ after the final convolution. The basis and testing functions are simple subsectional polynomials, and both the inner convolutions in (10.20)–(10.23) and the indicated differentiations are easily evaluated. The convolutions produce

$$T_{xm} * B_{xn} = aq(x; x_m - x_n - \frac{3}{2}a, x_m - x_n + \frac{3}{2}a) p(y; y_m - y_n - \frac{1}{2}b, y_m - y_n + \frac{1}{2}b) \quad (10.24)$$

$$T_{xm} * B_{yn} = at(x; x_m - x_n - a, x_m - x_n, x_m - x_n + a) t(y; y_m - y_n - b, y_m - y_n, y_m - y_n + b) \quad (10.25)$$

$$T_{ym} * B_{xn} = bt(x; x_m - x_n - a, x_m - x_n, x_m - x_n + a) t(y; y_m - y_n - b, y_m - y_n, y_m - y_n + b) \quad (10.26)$$

$$T_{ym} * B_{yn} = bp(x; x_m - x_n - \frac{1}{2}a, x_m - x_n + \frac{1}{2}a) q(y; y_m - y_n - \frac{3}{2}b, y_m - y_n + \frac{3}{2}b) \quad (10.27)$$

where the function q denotes a quadratic spline

$$q\left(x; -\frac{3a}{2}, \frac{3a}{2}\right) = \begin{cases} 0 & x < -\frac{3a}{2} \\ \frac{9}{8} + \frac{3x}{2a} + \frac{x^2}{2a^2} & -\frac{3a}{2} < x < -\frac{a}{2} \\ \frac{3}{4} - \frac{x^2}{a^2} & -\frac{a}{2} < x < \frac{a}{2} \\ \frac{9}{8} - \frac{3x}{2a} + \frac{x^2}{2a^2} & \frac{a}{2} < x < \frac{3a}{2} \\ 0 & x > \frac{3a}{2} \end{cases} \quad (10.28)$$

After carrying out the required differentiations, the expressions simplify to

$$\left(\frac{\partial^2}{\partial x^2} + k^2 \right) (T_{xm} * B_{xn}) = \left\{ \frac{1}{a} p \left(x; -\frac{3a}{2}, -\frac{a}{2} \right) - \frac{2}{a} p \left(x; -\frac{a}{2}, \frac{a}{2} \right) \right. \\ \left. + \frac{1}{a} p \left(x; \frac{a}{2}, \frac{3a}{2} \right) + k^2 a q \left(x; -\frac{3a}{2}, \frac{3a}{2} \right) \right\} \Big|_{x=x-x_m+x_n} \\ p \left(y; y_m - y_n - \frac{b}{2}, y_m - y_n + \frac{b}{2} \right) \quad (10.29)$$

$$\frac{\partial^2}{\partial x \partial y} (T_{xm} * B_{yn}) = \frac{1}{b} \{ p(x; -a, 0) p(y; -b, 0) - p(x; -a, 0) p(y; 0, b) \\ - p(x; 0, a) p(y; -b, 0) + p(x; 0, a) p(y; 0, b) \} \Big|_{x=x-x_m+x_n, y=y-y_m+y_n} \quad (10.30)$$

$$\frac{\partial^2}{\partial x \partial y} (T_{ym} * B_{xn}) = \frac{1}{a} \{ p(x; -a, 0) p(y; -b, 0) - p(x; -a, 0) p(y; 0, b) \\ - p(x; 0, a) p(y; -b, 0) + p(x; 0, a) p(y; 0, b) \} \Big|_{x=x-x_m+x_n, y=y-y_m+y_n} \quad (10.31)$$

$$\left(\frac{\partial^2}{\partial y^2} + k^2 \right) (T_{ym} * B_{yn}) = p \left(x; x_m - x_n - \frac{a}{2}, x_m - x_n + \frac{a}{2} \right) \\ \left. \left\{ \frac{1}{b} p \left(y; -\frac{3b}{2}, -\frac{b}{2} \right) - \frac{2}{b} p \left(y; -\frac{b}{2}, \frac{b}{2} \right) + \frac{1}{b} p \left(y; -\frac{b}{2}, -\frac{3b}{2} \right) \right. \right. \\ \left. \left. + k^2 b q \left(y; -\frac{3b}{2}, \frac{3b}{2} \right) \right\} \right|_{y=y-y_m+y_n} \quad (10.32)$$

Finally, the entries of the impedance matrix can be obtained after convolving each of (10.29)–(10.32) with the Green's function of (10.17). To ensure high accuracy, these convolutions must be done by two-dimensional numerical quadrature. Only two types of integrals appear, those involving pulse functions and those involving the quadratic spline function. By exploiting the convolution properties, the dimension of the final integral is reduced to 2 without approximation.

The quadrature process is straightforward except in those cases where the source and observation regions overlap, resulting in a singularity in the integrand. This singularity has the form $1/R$ and can be extracted and integrated analytically, using

$$\int_{-\alpha}^{\alpha} dx' \int_{-\beta}^{\beta} dy' \frac{1}{\sqrt{(x-x')^2 + (y-y')^2}} \\ = (x+\alpha) \ln \left(\frac{y+\beta+R_{22}}{y-\beta+R_{21}} \right) + (x-\alpha) \ln \left(\frac{y-\beta+R_{11}}{y+\beta+R_{12}} \right) \quad (10.33) \\ + (y+\beta) \ln \left(\frac{x+\alpha+R_{22}}{x-\alpha+R_{12}} \right) + (y-\beta) \ln \left(\frac{x-\alpha+R_{11}}{x+\alpha+R_{21}} \right)$$

where

$$R_{11} = \sqrt{(x-\alpha)^2 + (y-\beta)^2} \quad (10.34)$$

$$R_{12} = \sqrt{(x-\alpha)^2 + (y+\beta)^2} \quad (10.35)$$

$$R_{21} = \sqrt{(x+\alpha)^2 + (y-\beta)^2} \quad (10.36)$$

$$R_{22} = \sqrt{(x+\alpha)^2 + (y+\beta)^2} \quad (10.37)$$

Once the current density is determined from the solution of Equation (10.11), the bistatic scattering cross section can be calculated according to the approach outlined in Chapter 1. For the plate geometry, assuming that the incident electric field has unity amplitude and the cell dimensions are smaller than $\lambda/10$, the scattering cross section can

be approximated as

$$\begin{aligned}\sigma(\theta, \phi) \cong & \frac{k^2 \eta^2}{4\pi} \left| \sum_{n=1}^M j_{xn} \cos \phi \cos \theta \Psi_n(\theta, \phi) + \sum_{n=M+1}^N j_{yn} \sin \phi \cos \theta \Psi_n(\theta, \phi) \right|^2 \\ & + \frac{k^2 \eta^2}{4\pi} \left| \sum_{n=1}^M -j_{xn} \sin \phi \Psi_n(\theta, \phi) + \sum_{n=M+1}^N j_{yn} \cos \phi \Psi_n(\theta, \phi) \right|^2\end{aligned}\quad (10.38)$$

where

$$\Psi_n(\theta, \phi) = abe^{jk \sin \theta (x_n \cos \phi + y_n \sin \phi)} \quad (10.39)$$

Although the use of equal-sized rectangular cells is somewhat restrictive, this approach has considerable computational advantages when treating plates that are on the order of a wavelength or greater in size. Consider a plate geometry conforming to the parallelogram-lattice illustrated in Figure 4.12. Because the translational symmetry in the plate geometry is preserved by the use of equal-sized cells arranged along a lattice, the submatrices **A**, **B**, **C**, and **D** in Equation (10.11) are *block Toeplitz* in form, that is, **A** has the structure

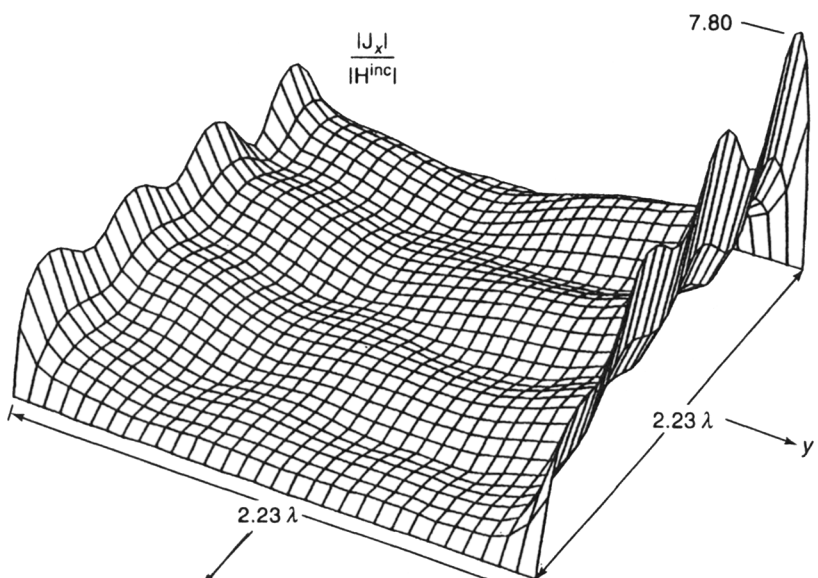
$$\mathbf{A} = \begin{bmatrix} \mathbf{A}_0 & \mathbf{A}_1 & \dots & \mathbf{A}_{P-1} \\ \mathbf{A}_1 & \mathbf{A}_0 & \dots & \mathbf{A}_{P-2} \\ \vdots & \vdots & \ddots & \vdots \\ \vdots & \vdots & & \vdots \\ \mathbf{A}_{P-1} & \mathbf{A}_{P-2} & \dots & \mathbf{A}_0 \end{bmatrix} \quad (10.40)$$

while each entry of (10.40) is itself a $Q \times Q$ Toeplitz matrix of the form

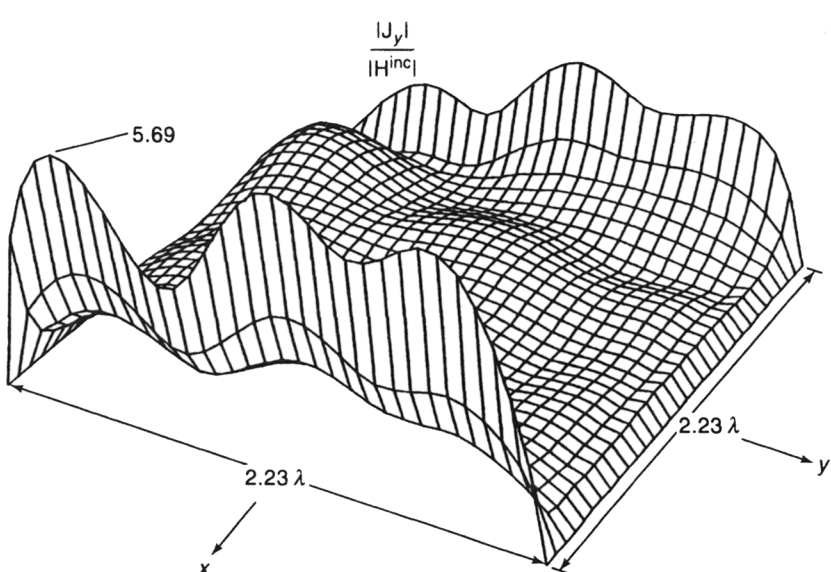
$$\mathbf{A}_i = \begin{bmatrix} a_0 & a_1 & \dots & a_{Q-1} \\ a_1 & a_0 & \dots & a_{Q-2} \\ \vdots & \vdots & \ddots & \vdots \\ \vdots & \vdots & & \vdots \\ a_{Q-1} & a_{Q-2} & \dots & a_0 \end{bmatrix} \quad (10.41)$$

Even if the plate geometry does not fill the entire lattice, there is a considerable amount of structure built into the matrix equation by the choice of equal-sized basis and testing functions. The redundancy can be exploited in two ways. First, only one row of each of the **A**, **B**, **C**, and **D** submatrices needs to be computed, as the other entries can be found from symmetry considerations. Since the two-dimensional numerical integration used to compute each matrix element is very time consuming, the computational savings are substantial. Second, due to the Toeplitz structure, the normal computer storage requirements can be greatly reduced during the solution process. This can be accomplished either by the use of specialized block Toeplitz algorithms [2] or by the use of an iterative algorithm (i.e., the CG-FFT approach discussed in Chapter 4). For illustration, Figure 10.5 presents the surface current density induced on a square plate of side dimension 2.23λ . This result was obtained using 1984 rooftop basis functions and a CG-FFT solution of Equation (10.11) [3].

To reduce the interpolation error associated with the basis expansion, the CN/LT rooftop basis functions used to represent the current density can be replaced with higher order functions, such as functions that provide a linear normal and quadratic tangential



(a)



(b)

Figure 10.5 The EFIE result for the surface current density on a square plate. The top view shows the x -component; the lower view shows the y -component. A plane wave with the electric field parallel to the plate is incident from the viewing angle. A total of 1984 CN/LT rooftop basis functions are used. After [3].

(LN/QT) behavior. The LN/QT functions within a rectangular cell consist of 12 functions (Section 9.13). For convenience, they can be defined on the reference cell ($-1 < \eta < 1$, $-1 < \xi < 1$) and mapped to general cell shapes by the procedure of Section 9.14. On the standard cell, four of these functions interpolate to the η -directed current along the cell edges at $\xi = -1$ and $\xi = 1$ and have the form

$$\hat{\eta} \left[\frac{1}{2}(1 \pm \xi) \frac{1}{2}(1 \pm \eta) \right] \quad (10.42)$$

Similarly, there are four basis functions representing the ξ -component:

$$\hat{\xi} \left[\frac{1}{2}(1 \pm \xi) \frac{1}{2}(1 \pm \eta) \right] \quad (10.43)$$

These eight functions each straddle two cells, with the normal component constrained to be continuous across the appropriate edge to ensure the absence of fictitious charge densities and maintain a finite surface divergence. There are four additional functions with support confined to the cell, which can be expressed as

$$\hat{n} \left[\frac{1}{2}(1 \pm \xi) \right] (1 + \eta)(1 - \eta) \quad (10.44)$$

$$\hat{\xi}(1 + \xi)(1 - \xi) \left[\frac{1}{2}(1 \pm \eta) \right] \quad (10.45)$$

These four functions contribute a quadratic tangential component along the cell edges and provide zero normal component. Therefore, they do not interfere with the interpolation properties of the functions defined in Equations (10.42) and (10.43). From a global perspective, there are two basis functions per non-boundary edge and two basis functions per cell throughout the plate model.

Razor-blade testing functions can be used to enforce the equations arising from the LN/QT expansion and can be defined with their domain of support as depicted in Figure 10.6. To illustrate the comparison of the CN/LT and LN/QT expansions, Figures 10.7 and 10.8 show the current density induced on a $1\lambda \times 1\lambda$ plate by a uniform plane wave [4]. Both expansions appear to produce similar results for $N = 480$. In fact, for the plate geometry, the accuracy seems to be limited primarily by the need to incorporate the proper edge singularity into the representation. Since neither CN/LT nor LN/QT basis functions provide a tangential current with the proper square root singularity [5]

$$J_{\tan} \approx O \left(\frac{1}{\sqrt{u}} \right) \quad \text{as } u \rightarrow 0 \quad (10.46)$$

near the plate's edge, it is difficult to judge relative accuracy.

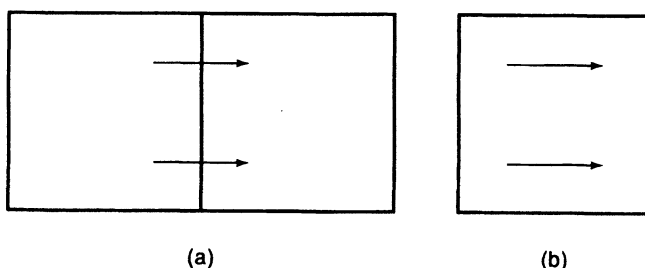


Figure 10.6 Domain of support for the razor-blade testing functions used with the LN/QT basis functions on a standard square cell: (a) paths for the two edge-based functions; (b) paths for two of the four cell-based functions.

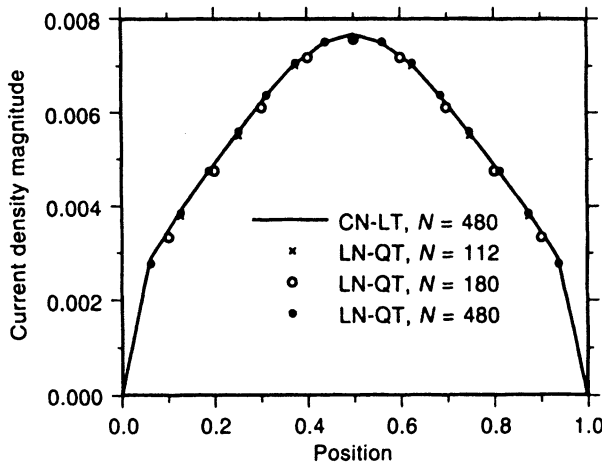


Figure 10.7 Comparison of the copolarized current density tangential to a line through the center of a $1\lambda \times 1\lambda$ plate. The EFIE result obtained using 480 CN/LT basis functions is compared with results obtained using 112, 180, and 480 LN/QT basis functions. After [4]. ©1996 American Geophysical Union.

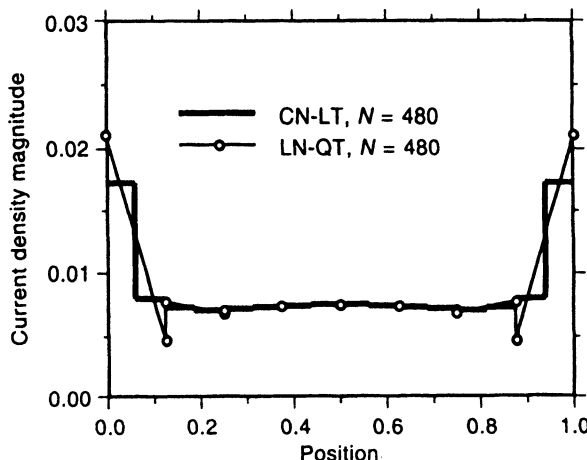


Figure 10.8 Comparison of the copolarized current density normal to a line through the center of a $1\lambda \times 1\lambda$ plate for 480 CN/LT and 480 LN/QT functions. After [4]. ©1996 American Geophysical Union.

Both the CN/LT and LN/QT functions provide a discontinuous representation of the current density, since they only impose continuity of the normal component between cells. For a regular discretization of the plate geometry, such as used to obtain the data shown in Figures 10.7 and 10.8, the tangential discontinuities tend to be small except near the plate edge, where the erratic behavior of the numerical solution is expected due to the incorrect edge singularity [5]. For irregular discretizations, the numerical solution is likely to contain noticeable discontinuities in the tangential current component at cell boundaries. Of course, these discontinuities should disappear as the cell dimensions are reduced.

The preceding EFIE formulation illustrates several special properties arising in the analysis of planar structures, including the use of convolutions to improve the efficiency of the matrix fill and discrete convolutions to improve the matrix solution efficiency. These properties have been exploited when modeling planar devices such as microstrip antennas and feed structures [6, 7] and frequency-selective surfaces [8]. However, for nonplanar objects greater flexibility is provided through the use of triangular-cell shapes. The following section considers a triangular-cell EFIE approach for scattering from plates and arbitrary conducting bodies.

10.2 SCATTERING FROM PERFECTLY CONDUCTING BODIES: EFIE DISCRETIZED WITH CN/LT TRIANGULAR-CELL ROOFTOP BASIS FUNCTIONS [9]

For scatterers of arbitrary shape, triangular cells offer the possibility of a self-consistent three-dimensional model with variable cell sizes (Figure 10.9). Consider a generalization of the previous formulation using the tangential projection of the mixed-potential EFIE

$$\bar{E}^{\text{inc}}(u, v) = jk\eta\bar{A}(u, v) + \nabla\Phi_e \quad (10.47)$$

where

$$\bar{A}(u, v) = \iint \bar{J}(u', v') \frac{e^{-jkR}}{4\pi R} du' dv' \quad (10.48)$$

$$\Phi_e(u, v) = \frac{1}{\epsilon_0} \iint \rho_e(u', v') \frac{e^{-jkR}}{4\pi R} du' dv' \quad (10.49)$$

$$R = \sqrt{[x(u, v) - x(u', v')]^2 + [y(u, v) - y(u', v')]^2 + [z(u, v) - z(u', v')]^2} \quad (10.50)$$

and (u, v) denote parametric coordinates along the surface of the conducting scatterer. The surface charge density is related to the current by the continuity equation

$$\rho_e = \frac{1}{j\omega} \nabla_s \cdot \bar{J} \quad (10.51)$$

The mixed-potential form of the EFIE proves advantageous for general-shaped scatterers, since it facilitates the explicit transfer of one derivative to the basis functions for \bar{J} and another to the testing functions.

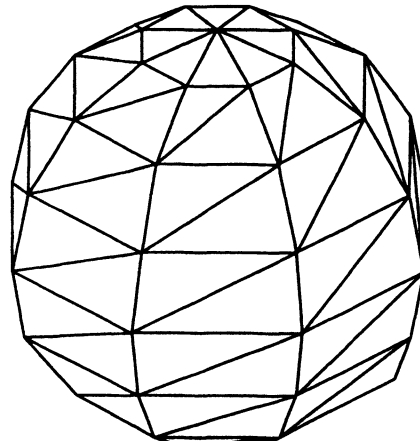


Figure 10.9 Triangular-patch model of a sphere.

A triangular-cell representation of the surface current density can be obtained using the *triangular-rooftop* CN/LT vector basis function introduced in Section 9.13 (Figure 9.24). Each rooftop function spans two adjacent triangles and interpolates to the vector component of the current density normal to the common edge. For a scatterer model with N edges, the current density can be expanded in N basis functions

$$\bar{J}(u, v) \cong \sum_{n=1}^N j_n \bar{B}_n(u, v) \quad (10.52)$$

where $\{j_n\}$ represents the unknown coefficients. Each coefficient can be interpreted as the current flowing across a particular edge. In addition to imposing continuity of the normal component along the common edge of the cell pair, each basis function also has a vanishing normal component along the other four edges. Thus, a triangular-rooftop function eliminates jump discontinuities in \bar{J} that produce fictitious charges at cell edges [9]. In other words, because the normal component of the current density is continuous along the surface, the surface divergence of the expansion is always finite. Consider basis function $\bar{B}_n(u, v)$ associated with edge n , spanning cells i and j , with the vector direction from cell i into cell j . From Equation (9.264), we obtain

$$\nabla_s \cdot \bar{B}_n = \frac{w_n}{A_i} p_i(u, v) - \frac{w_n}{A_j} p_j(u, v) \quad (10.53)$$

where w_n is the length of edge n , A_i is the area of cell i , and $p_i(u, v)$ denotes a pulse function with support confined to cell i . Thus, the surface charge density associated with a rooftop basis function is a piecewise-constant charge doublet.

To discretize the EFIE, we seek testing functions that (1) provide the proper differentiability requirements and (2) are compatible with the triangular-cell representation. Ideally, the testing functions should also be centered at cell edges. The razor-blade functions used in the preceding section can be generalized to meet these requirements. Suppose cells i and j share edge m . The domain of a razor-blade function $\bar{T}_m(u, v)$ can be restricted to the straight-line path along the scatterer surface from the centroid of cell i to the midpoint of edge m and then along a second straight-line path to the centroid of cell j (Figure 10.10). Each testing function is a vector tangential to the path, oriented in a direction specified by the scatterer model. (In practice, the model includes a connectivity array linking edge indices to the two adjacent cell indices and simultaneously specifying the vector direction of the basis and testing function defined at each edge.)

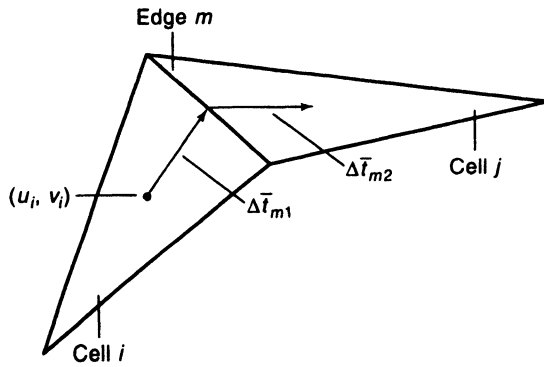


Figure 10.10 Domain of the razor-blade testing function associated with edge m in a triangular-patch model of a surface.

After substituting basis and testing functions into the EFIE, we obtain the matrix equation $\mathbf{A}\mathbf{j} = \mathbf{b}$, with entries

$$\begin{aligned} A_{mn} &= jk\eta \int_{C_m} \left(\iiint \bar{B}_n(u', v') \frac{e^{-jkR}}{4\pi R} du' dv' \right) \cdot d\bar{t} \\ &\quad + \frac{\eta}{jk} \int_{C_m} \nabla \left(\iiint [\nabla_s \cdot \bar{B}_n] \frac{e^{-jkR}}{4\pi R} du' dv' \right) \cdot d\bar{t} \end{aligned} \quad (10.54)$$

$$b_m = \int_{C_m} \bar{E}^{\text{inc}} \cdot d\bar{t} \quad (10.55)$$

where C_m denotes the particular path from (u_i, v_i) to (u_j, v_j) associated with the testing function at edge m (Figure 10.10). In (10.54) and throughout this chapter, the divergence $[\nabla_s \cdot \bar{B}_n]$ is carried out in primed coordinates.

The second integral in (10.54) can be simplified using the identity

$$\int_{C_m} \nabla \Phi \cdot d\bar{t} = \Phi(u_j, v_j) - \Phi(u_i, v_i) \quad (10.56)$$

to eliminate the integral along C_m and the gradient operation. The first integral in (10.54) can also be simplified using the approximation

$$\int_{C_m} \bar{A} \cdot d\bar{t} \cong \bar{A} \cdot \Delta \bar{t}_{m1} \Big|_{u_i, v_i} + \bar{A} \cdot \Delta \bar{t}_{m2} \Big|_{u_j, v_j} \quad (10.57)$$

to eliminate the integral along C_m . In (10.57), $\Delta \bar{t}_{m1}$ denotes the vector from the centroid of cell i to the center of edge m , and $\Delta \bar{t}_{m2}$ denotes the vector from the center of edge m to the centroid of cell j , where i and j are the two cells associated with edge m (Figure 10.10). With these simplifications, the matrix entries can be written as

$$\begin{aligned} A_{mn} \cong & jk\eta \left(\Delta \bar{t}_{m1} \cdot \iint \bar{B}_n(u', v') \frac{e^{-jkR}}{4\pi R} du' dv' \Big|_{u_i, v_i} \right. \\ & \left. + \Delta \bar{t}_{m2} \cdot \iint \bar{B}_n(u', v') \frac{e^{-jkR}}{4\pi R} du' dv' \Big|_{u_j, v_j} \right) \\ & + \frac{\eta}{jk} \left(\iint [\nabla_s \cdot \bar{B}_n] \frac{e^{-jkR}}{4\pi R} du' dv' \Big|_{u_j, v_j} \right. \\ & \left. - \iint [\nabla_s \cdot \bar{B}_n] \frac{e^{-jkR}}{4\pi R} du' dv' \Big|_{u_i, v_i} \right) \end{aligned} \quad (10.58)$$

where (u_i, v_i) denotes the centroid of cell i . The integrals in (10.58) are expressed over the entire scatterer surface, but they obviously collapse to the support of the two cells associated with the basis function at edge n . In general, these integrals must be evaluated by numerical quadrature. When the source and observation regions overlap, the $1/R$ singularity may be extracted and integrated analytically, in a manner similar to that described in Section 10.1. The procedure has been detailed in recent publications [10, 11].

The scatterer model required to implement the above procedure consists of a list of the coordinates (x, y, z) of the corner of each cell (the *nodes*) and several pointer arrays specifying the connectivity between cells, edges, and nodes. Specifically, the direct evaluation of A_{mn} requires a pointer to identify the two cells adjacent to each edge where a basis function resides (and the orientation of that basis function) as well as a second pointer to identify the three nodes associated with each cell. Other needed parameters such as the centroid coordinates and the vectors $\Delta \bar{t}_{m1}$ and $\Delta \bar{t}_{m2}$ can be obtained from the given information.

The entry A_{mn} in (10.58) involves four integrals over each of the two cells adjacent to edge n , with observer locations fixed at the centroids of the two cells adjacent to edge m . By considering the possible combinations of source and observer locations, it is easily concluded that many of these individual integrals are repeated within the matrix entries for basis and testing functions at nearby edges. In fact, the independent calculation of each A_{mn} requires approximately nine times the computation that would be necessary if each integral was performed only once [9]. To minimize the time-consuming numerical quadrature, each integral can be evaluated once for each cell and observer location and

added to the appropriate entry in the A -matrix using the connectivity information provided by the scatterer model. (This indirect way of constructing the matrix has been described in detail in connection with the finite-element procedure in Chapter 3.) This approach may require a scatterer model with slightly different connectivity arrays than those required for the naive calculation of each A_{mn} .

To illustrate the approach, Figure 10.11 shows the surface current density induced on a one-wavelength plate using the triangular-cell EFIE formulation with CN/LT basis functions. For comparison, results from a rectangular-cell CN/LT approach similar to that presented in Section 10.1 are also shown. Other results demonstrating the validity of the triangular-cell approach for a variety of scatterer shapes may be found in the literature [8, 9]. We leave the development of expressions for the scattering cross section to the readers.

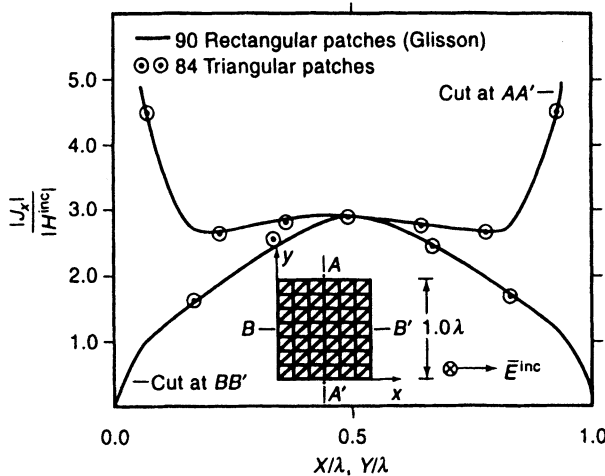


Figure 10.11 The EFIE result for the dominant current component on a $1\lambda \times 1\lambda$ plate, obtained with triangular-cell CN/LT functions and rectangular-cell CN/LT functions. After [9]. ©1982 IEEE.

In practice, the substantial computational requirements of three-dimensional analysis motivates a reduction in the number of unknowns by any available means. Often, geometrical symmetries such as reflection symmetry or rotational symmetry can be exploited. Reference [12] provides an overview of a number of common geometrical symmetries that can be used to enhance the efficiency of solution.

10.3 SCATTERING FROM PERFECTLY CONDUCTING BODIES: MFIE DISCRETIZED WITH TRIANGULAR-CELL CN/LT BASIS FUNCTIONS

For closed p.e.c. bodies, a solution can also be obtained using the MFIE

$$\hat{n} \times \bar{H}^{\text{inc}} = \bar{J} - \hat{n} \times \nabla \times \bar{A} \Big|_{S^+} \quad (10.59)$$

where \hat{n} denotes the outward normal vector, \bar{A} is the magnetic vector potential

$$\bar{A}(u, v) = \iint \bar{J}(u', v') \frac{e^{-jkR}}{4\pi R} du' dv' \quad (10.60)$$

R is given by

$$R = \sqrt{[x(u, v) - x(u', v')]^2 + [y(u, v) - y(u', v')]^2 + [z(u, v) - z(u', v')]^2} \quad (10.61)$$

and (u, v) are parametric variables defined along the scatterer surface. The S^+ in (10.59) is a reminder that the MFIE is to be evaluated an infinitesimal distance outside the surface.

Suppose that the scatterer surface is discretized into triangular cells and the CN/LT triangular-rooftop functions employed in Section 10.2 are used to represent the current, namely,

$$\bar{J}(u, v) \cong \sum_{n=1}^N j_n \bar{B}_n(u, v) \quad (10.62)$$

Since the rooftop functions interpolate to the normal vector component at each edge, the coefficient j_n can be interpreted as the surface current density flowing across edge n .

A simple method-of-moments discretization can be obtained by point matching Equation (10.59) at the center of each edge in the vector direction given by the razor-blade functions used in Section 10.2. Such a testing procedure involves the components of \bar{H}^{inc} and \bar{H}^s parallel to each edge and the component of \bar{J} perpendicular to each edge. These quantities are all continuous and well defined at the edges. This approach produces the matrix equation $C\mathbf{j} = \mathbf{d}$, where

$$\begin{aligned} C_{mn} &= -\hat{e}_m \cdot \nabla \times \iint \bar{B}_n(u', v') \frac{e^{-jkR}}{4\pi R} du' dv' \Big|_{u_m, v_m} \\ &= \hat{e}_m \cdot \iint \bar{B}_n(u', v') \times \nabla \left(\frac{e^{-jkR}}{4\pi R} \right) du' dv' \Big|_{u_m, v_m} \quad m \neq n \end{aligned} \quad (10.63)$$

$$\begin{aligned} C_{mm} &= 1 - \lim_{u, v \rightarrow u_m^+, v_m^+} \left(\hat{e}_m \cdot \nabla \times \iint \bar{B}_m(u', v') \frac{e^{-jkR}}{4\pi R} du' dv' \right) \\ &= \frac{2\pi - \Omega_m}{2\pi} \end{aligned} \quad (10.64)$$

and

$$d_m = \hat{e}_m \cdot \bar{H}^{\text{inc}} \Big|_{u_m, v_m} \quad (10.65)$$

where Ω_m denotes the interior angle subtended by the cell pair at edge m and \hat{e}_m denotes a unit vector parallel to edge m and oriented so that $\hat{n} \times \hat{e}_m$ points in the same direction as the basis function \bar{B}_m .

The numerical evaluation of (10.63) is straightforward for flat-cell models since the integrand is never singular. [In the case of basis and testing functions located at different edges of the same cell, the contribution to (10.63) vanishes due to the property that there is no tangential magnetic field produced in the same plane as the source current.] The scatterer model can be described by a list of nodes and several connectivity arrays, as discussed in Section 10.2. It may be convenient to include the direction of each vector \hat{e}_m within the model; otherwise some mechanism must be provided to specify the outward normal direction for every cell.

10.4 SCATTERING FROM PERFECTLY CONDUCTING BODIES: CFIE DISCRETIZED WITH TRIANGULAR-CELL CN/LT BASIS FUNCTIONS

To circumvent internal resonance difficulties (Chapter 6) that might occur with closed three-dimensional scatterers, the EFIE formulation from Section 10.2 and the MFIE approach from Section 10.3 can be brought together to produce a CFIE formulation. In common with the two-dimensional CFIE, the three-dimensional CFIE is a simple linear combination of the EFIE and MFIE. The simplest approach is to work directly with the matrix entries for the EFIE and MFIE presented in the two preceding sections. The CFIE approach produces the $N \times N$ system $\mathbf{Ej} = \mathbf{f}$, where

$$E_{mn} = \alpha A_{mn} + (1 - \alpha)\eta \Delta t_m C_{mn} \quad (10.66)$$

and

$$f_m = \alpha b_m + (1 - \alpha)\eta \Delta t_m d_m \quad (10.67)$$

In these equations, η denotes the intrinsic impedance of the background medium and Δt_m is the length of path C_m associated with a razor-blade testing function from Section 10.2. These factors serve to scale the numerical entries of the EFIE and MFIE to obtain similar values regardless of the cell sizes. Matrix entries A_{mn} , b_m , C_{mn} , and d_m are defined in Equations (10.58), (10.55), and (10.63)–(10.65). The parameter α is a variable in the range $0 < \alpha < 1$ that can be used to adjust the relative weighting of the EFIE and MFIE as explained in Chapter 6.

Alternative approaches for eliminating the internal resonances (such as the combined-source and the dual-surface formulations introduced in Chapter 6) are also possible for three-dimensional conducting bodies, and we leave their development to the reader.

10.5 PERFORMANCE OF THE CFIE WITH LN/QT BASIS FUNCTIONS AND CURVED PATCHES [4]

In this section, the CFIE formulation is extended to incorporate a curved-patch scatterer model. The EFIE matrix entries are computed according to the expressions in (9.319)–(9.321), while the MFIE matrix entries are computed according to

$$\iint \bar{T}_m \cdot \bar{H}^s dS = \int_{\eta} \int_{\xi} \int_{\xi'} [T_{\eta} T_{\xi}]_m \mathbf{J}_m \begin{bmatrix} 0 & -\frac{\partial G}{\partial z} & \frac{\partial G}{\partial y} \\ \frac{\partial G}{\partial z} & 0 & -\frac{\partial G}{\partial x} \\ -\frac{\partial G}{\partial y} & \frac{\partial G}{\partial x} & 0 \end{bmatrix} \mathbf{J}_n^T \begin{bmatrix} B_{\eta} \\ B_{\xi} \end{bmatrix}_n d\eta' d\xi' d\eta d\xi \quad (10.68)$$

where \mathbf{J} is the Jacobian matrix defined in (9.314) and B_{η} and B_{ξ} denote the contravariant components of the basis function in the reference cell. The testing and basis functions are defined using the scaled contravariant projection in (9.317). For a triangular reference cell, the integration limits in (9.319)–(9.321) and (10.68) are modified accordingly. The Green's function singularity within the EFIE can be extracted and integrated in closed form over a planar cell tangent to the curved patch, as described in previous sections.

Curved patches can be realized using a mapping based on the triangular-cell quadratic scalar Lagrangian interpolation polynomials in (9.15)–(9.20). The cell location is defined by

$$x = \sum_{i=0}^2 \sum_{j=0}^2 x_{ijk} B_{ijk}(L_1, L_2, L_3) \quad (10.69)$$

$$y = \sum_{i=0}^2 \sum_{j=0}^2 y_{ijk} B_{ijk}(L_1, L_2, L_3) \quad (10.70)$$

$$z = \sum_{i=0}^2 \sum_{j=0}^2 z_{ijk} B_{ijk}(L_1, L_2, L_3) \quad (10.71)$$

where (L_1, L_2, L_3) denote simplex coordinates (Section 9.1), $k = 2 - i - j$ (with $k = 0, 1, 2$), and the nodes $(x_{ijk}, y_{ijk}, z_{ijk})$ describe the corners and midside coordinates of the curved patch. This mapping produces a doubly parabolic patch shape.

For illustration, a specific discretization can be obtained using the LN/QT basis functions introduced in Section 9.13 (Figure 9.25) and razor-blade testing functions defined along paths that roughly correspond to the basis function locations (Figure 10.12). A 112-cell model of a sphere is shown in Figure 10.9; Figures 10.13 and 10.14 show the dominant currents induced on a perfectly conducting sphere of radius 0.6λ using a similar 112-cell curved-patch model. On average, a density of approximately $124 \text{ unknowns}/\lambda^2$ was provided by this model.

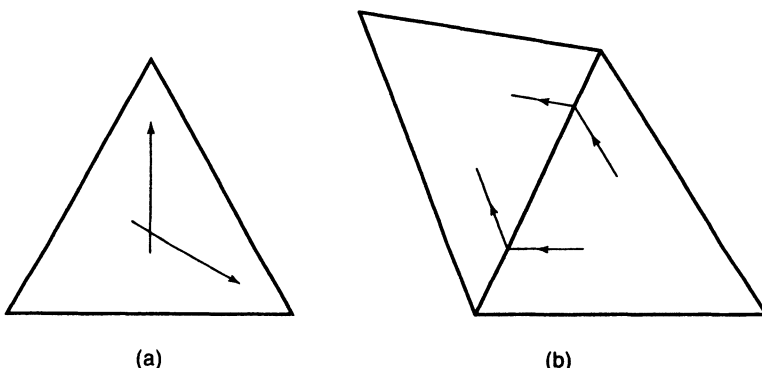


Figure 10.12 Domain of support for the razor-blade testing functions used with the LN/QT basis functions on triangular cells: (a) paths for the two cell-based functions; (b) paths for the edge-based functions.

Figures 10.13 and 10.14 show the magnitude of \bar{J}_θ and \bar{J}_ϕ as a function of θ , assuming that the incident field propagates in the $\theta = 180^\circ$ direction and has an electric field polarized in the $-\hat{x}$ direction. To produce the maximum values of \bar{J}_θ and \bar{J}_ϕ , respectively, Figure 10.13 depicts the $\phi = 0^\circ$ cut while Figure 10.14 depicts the $\phi = 90^\circ$ cut. The results generally exhibit good agreement with the exact solutions, although they contain slight discontinuities (more pronounced in \bar{J}_ϕ) at cell junctions. As discussed in previous sections, the divergence-conforming basis functions ensure the continuity of the normal current density across cells but allow jump discontinuities in the tangential current density. In an irregular-grid model, a general cut through the mesh is likely to cross cell bound-

aries at skew angles, and thus the currents displayed in these plots contain both normal and tangential components. Consequently, some discontinuities are expected in the numerical results.

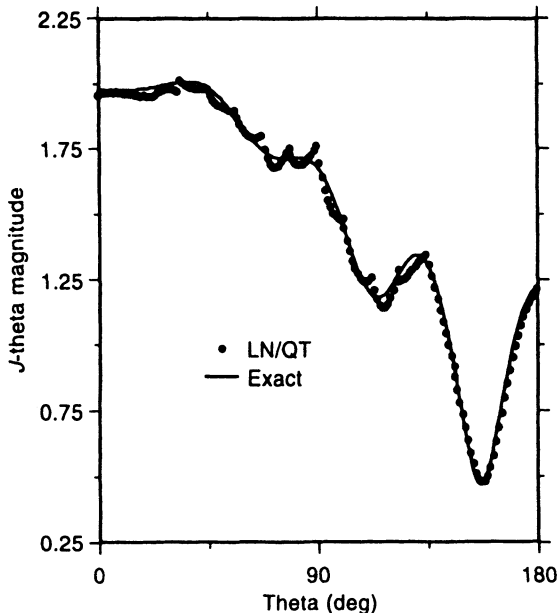


Figure 10.13 Dominant θ -component of the current density induced on a sphere of radius 0.6λ by an incident plane wave. The CFIE result is obtained using a 112-cell curved triangular-patch model involving a density of approximately 124 LN/QT unknowns per square wavelength. After [4]. ©1996 American Geophysical Union.

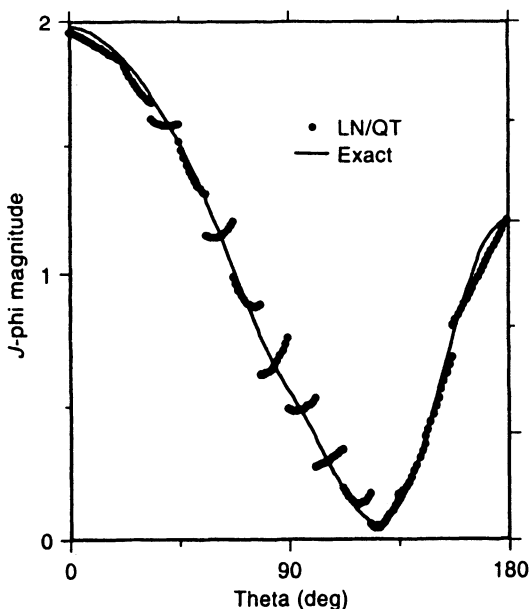


Figure 10.14 Dominant ϕ -component of the current density induced on a sphere of radius 0.6λ by an incident plane wave. The CFIE result is obtained using a 112-cell curved triangular-patch model involving a density of approximately 124 LN/QT unknowns per square wavelength. After [4]. ©1996 American Geophysical Union.

10.6 TREATMENT OF ELECTRICALLY SMALL SCATTERERS USING SURFACE INTEGRAL EQUATIONS

Chapter 6 discussed a difficulty with EFIE formulations when used to analyze a closed scatterer near an interior resonance frequency. Another difficulty with EFIE formulations arises when the equation is used near the low-frequency limit (i.e., for a scatterer geometry that is very small in terms of wavelengths). If the geometry is such that current is permitted to flow in closed loops, the EFIE will fail as the electrical size of the geometry tends to zero. Consequently, for geometries much smaller than a wavelength, a conventional EFIE discretization produces a highly ill-conditioned system of equations. In the two-dimensional situation, the difficulty only arises for the TE polarization. An eigenvalue interpretation for circular cylinders (Chapter 5) suggests that as the cylinder radius approaches zero, one eigenvalue of the TE EFIE operator approaches the origin while the rest tend to infinity! Clearly, numerical solution methods will not be able to cope with such a situation, in two or three dimensions, without special features.

The difficulty can be illustrated by considering the “mixed-potential” form of the EFIE

$$\hat{n} \times \bar{E}^{\text{inc}} = jk\eta\hat{n} \times \bar{A} + \hat{n} \times \nabla\Phi \quad (10.72)$$

As the scatterer becomes small compared to the wavelength, the numerical contribution from the $\nabla\Phi$ term of Equation (10.72) dominates the contribution from the magnetic vector potential \bar{A} . Since the scalar potential Φ depends only on the surface charge density, the EFIE decouples from the current density \bar{J} as the contribution from \bar{A} decreases. Fundamentally, this behavior is related to the decoupling of the electric field and charge density from the magnetic field and current density in the static limit. The conventional EFIE involves the incident electric field and can sometimes be used to describe the electrostatic situation; it does not incorporate the incident magnetic field and therefore cannot be used to analyze the magnetostatic situation. For electrically small scatterers whose characterization requires both electrostatic and magnetostatic contributions, the EFIE will fail.

If the scatterer geometry is such that the current density can flow in closed loops, the ordinary method-of-moments matrix operator obtained from the EFIE will become singular as the scatterer size shrinks to zero. Although the matrix is constructed using N linearly independent basis functions for \bar{J} , the corresponding representation of the charge density does not generally have N independent degrees of freedom. As an illustration, consider a plate discretized into rectangular cells (Figure 10.15). If rooftop basis functions are employed to discretize the current within the EFIE following the approach discussed in Section 10.1, the specific geometry of Figure 10.15 requires 37 basis functions for \bar{J} . The charge density associated with the rooftop functions is constant within each cell. However, there are only 24 cells in the plate (and since the total net charge is constrained to vanish because of the nature of the rooftop functions, there are only 23 degrees of freedom associated with the charge representation). Therefore, as the scatterer size tends to zero and the contribution from the magnetic vector potential is dominated by that of the scalar potential, the rank of the method-of-moments matrix will collapse from 37 to 23 for the plate example.

An alternative interpretation of the difficulty is found by examining the testing process used to discretize the EFIE. For the plate formulation of Section 10.1, razor-blade testing

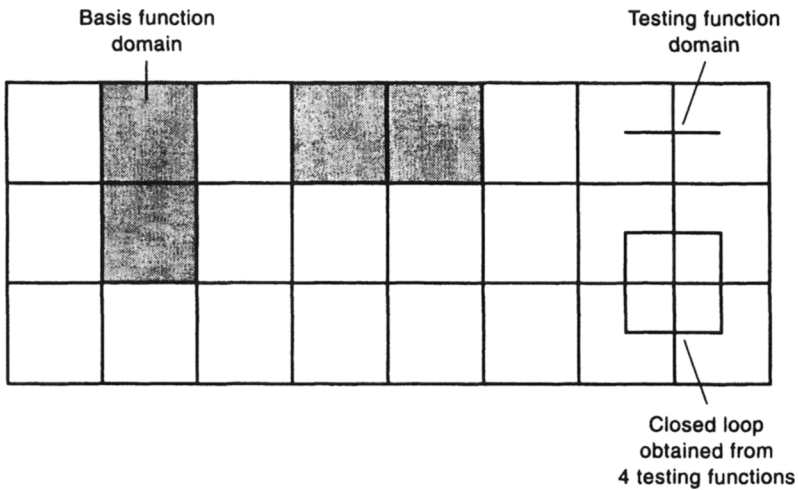


Figure 10.15 Plate discretized into 24 cells, showing the domain of a single testing function and the combined domain of four testing functions in a loop.

functions were employed with CN/LT rooftop basis functions. Each testing function straddles adjacent cells, so that there are 37 required with the plate of Figure 10.15. As the contribution from the magnetic vector potential is reduced, the net effect of “testing” the EFIE from the center of one cell to the center of the next is that the gradient $\nabla\Phi$ is integrated around closed loops. However, a vector identity states that

$$\int_{\text{any closed path}} \nabla\Phi \cdot d\vec{t} = 0 \quad (10.73)$$

Thus, not all of the matrix rows are independent. (The number of closed loops, 14, is exactly the difference between the number of independent current basis functions and the effective number of basis functions used for the charge density.)

As a general rule, most surface EFIE formulations will fail as the scatterer size is reduced beyond some limit because of the lack of sufficient information concerning the magnetostatic part of the problem. Several remedies have been proposed [13–16].

One remedy is motivated by a modification of the testing procedure used with the EFIE for the plate example [13, 14]. In the modified procedure, three of the four testing functions used to construct each closed loop are employed as usual, but the fourth equation is constructed by integrating only the magnetic vector potential term around the entire closed loop. This approach eliminates the round-off error due to the difference in size of the scalar and vector potential contributions to the matrix equation. In addition, by integrating the EFIE around a closed loop, the incident electric field can be explicitly replaced with its circulation (a component of the incident magnetic field). In essence, some of the matrix rows of the original EFIE formulation are replaced by equations obtained from a normal-component MFIE. Consequently, this modified formulation explicitly incorporates information enabling it to treat the magnetostatic part of the problem. The procedure generalizes to arbitrarily shaped scatterers. Furthermore, this approach can be employed regardless of scatterer size and requires no increase in computation over the conventional EFIE for a given scatterer model [13, 14].

As discussed in Chapter 5, an eigenvalue interpretation of the EFIE for circular TE cylinders indicates that one eigenvalue vanishes as the cylinder radius tends to zero while the others become infinite. For the circular cylinder example, the eigenfunction associated with the zero eigenvalue is a constant function. In general, the magnetostatic part of the current density always involves functions having zero divergence. Alternative formulations for electrically small scatterers [15, 16] typically employ a basis that explicitly separates the magnetostatic part of the current (which has zero divergence) from the electrostatic part (consisting of the rest of the current distribution). In the vector case, divergence-conforming loop and star functions (Section 9.9) can be used to facilitate this partitioning. By explicitly separating the magnetostatic part of the current density, a variety of stable numerical formulations can be constructed. Additional details may be found in the literature [15, 16].

10.7 SCATTERING FROM HOMOGENEOUS DIELECTRIC BODIES: CFIE DISCRETIZED WITH TRIANGULAR-CELL CN/LT BASIS FUNCTIONS [17]

A homogeneous three-dimensional dielectric body with permittivity ε_d and permeability μ_d can be characterized by coupled surface integral equations in terms of equivalent electric and magnetic currents on the scatterer surface. To avoid difficulties associated with interior resonances, a CFIE formulation can be constructed as an alternative to the coupled electric or magnetic field equations introduced in Section 1.9. Recall that the surface integral formulation is based on two equivalent problems, an exterior problem and an interior problem. By rearranging terms in (1.111), (1.112), (1.117), and (1.118), we obtain the equations associated with the exterior equivalent problem in the form

$$\bar{K} = -\hat{n} \times \bar{E}^{\text{inc}} - \hat{n} \times \left\{ \frac{\eta}{jk} (\nabla \nabla \cdot \bar{A} + k^2 \bar{A}) - \nabla \times \bar{F} \right\}_{S^+} \quad (10.74)$$

$$\bar{J} = \hat{n} \times \bar{H}^{\text{inc}} + \hat{n} \times \left\{ \nabla \times \bar{A} + \frac{\nabla \nabla \cdot \bar{F} + k^2 \bar{F}}{jk\eta} \right\}_{S^+} \quad (10.75)$$

and the equations associated with the interior equivalent problem in the form

$$\bar{K} = \hat{n} \times \left\{ \frac{\eta_d}{jk_d} (\nabla \nabla \cdot \bar{A}_d + k_d^2 \bar{A}_d) - \nabla \times \bar{F}_d \right\}_{S^-} \quad (10.76)$$

$$\bar{J} = -\hat{n} \times \left\{ \nabla \times \bar{A}_d + \frac{\nabla \nabla \cdot \bar{F}_d + k_d^2 \bar{F}_d}{jk_d \eta_d} \right\}_{S^-} \quad (10.77)$$

where \bar{J} and \bar{K} are the equivalent exterior electric and magnetic surface current densities, \hat{n} is the outward normal vector, \bar{A} and \bar{F} are the magnetic and electric vector potential functions

$$\bar{A}(u, v) = \iint \bar{J}(u', v') \frac{e^{-jkR}}{4\pi R} du' dv' \quad (10.78)$$

$$\bar{F}(u, v) = \iint \bar{K}(u', v') \frac{e^{-jkR}}{4\pi R} du' dv' \quad (10.79)$$

in the exterior medium, and \bar{A}_d and \bar{F}_d are the vector potential functions

$$\bar{A}_d(u, v) = \iint \bar{J}(u', v') \frac{e^{-jk_d R}}{4\pi R} du' dv' \quad (10.80)$$

$$\bar{F}_d(u, v) = \iint \bar{K}(u', v') \frac{e^{-jk_d R}}{4\pi R} du' dv' \quad (10.81)$$

in the dielectric material. Equations (10.74) and (10.75) are to be evaluated an infinitesimal distance *outside* the scatterer surface (S^+), while Equations (10.76) and (10.77) are to be evaluated an infinitesimal distance *inside* the surface (S^-).

To obtain combined-field equations, we equate (10.74) and (10.76) to obtain

$$\begin{aligned} -\hat{n} \times \bar{E}^{\text{inc}} &= \hat{n} \times \left\{ \frac{\eta}{jk} (\nabla \nabla \cdot \bar{A} + k^2 \bar{A}) - \nabla \times \bar{F} \right\}_{S^+} \\ &\quad + \hat{n} \times \left\{ \frac{\eta_d}{jk_d} (\nabla \nabla \cdot \bar{A}_d + k_d^2 \bar{A}_d) - \nabla \times \bar{F}_d \right\}_{S^-} \end{aligned} \quad (10.82)$$

and equate (10.75) and (10.77) to obtain

$$\begin{aligned} -\hat{n} \times \bar{H}^{\text{inc}} &= \hat{n} \times \left\{ \nabla \times \bar{A} + \frac{\nabla \nabla \cdot \bar{F} + k^2 \bar{F}}{jk\eta} \right\}_{S^+} \\ &\quad + \hat{n} \times \left\{ \nabla \times \bar{A}_d + \frac{\nabla \nabla \cdot \bar{F}_d + k_d^2 \bar{F}_d}{jk_d \eta_d} \right\}_{S^-} \end{aligned} \quad (10.83)$$

Together, Equations (10.82) and (10.83) constitute a combined-field formulation that will produce unique solutions even at frequencies where the conventional EFIE or MFIE fails because of interior resonance difficulties.

We again consider a triangular-cell model for the scatterer surface and represent the unknown electric and magnetic surface current densities by the CN/LT triangular-rooftop basis functions used in previous sections. For a model with N edges, the currents can be written

$$\bar{J}(u, v) \cong \sum_{n=1}^N j_n \bar{B}_n(u, v) \quad (10.84)$$

$$\bar{K}(u, v) \cong \sum_{n=1}^N k_n \bar{B}_n(u, v) \quad (10.85)$$

Equations (10.82) and (10.83) can be discretized using the razor-blade testing functions illustrated in Figure 10.10, which each have support along a path from the centroid of one cell to the centroid of an adjacent cell. Because the razor-blade testing functions are only capable of absorbing one derivative, the vector potential terms $\nabla \cdot \bar{A}$ and $\nabla \cdot \bar{F}$ in (10.82) and (10.83) can be replaced with equivalent scalar potential functions (Section 1.4), which is essentially the same as replacing the source-field relation embodied in these equations in order to transfer one derivative onto the surface currents. The result of the discretization is a matrix equation having the form

$$\begin{bmatrix} \mathbf{A} & \mathbf{B} \\ \mathbf{C} & \mathbf{D} \end{bmatrix} \begin{bmatrix} \mathbf{j} \\ \mathbf{k} \end{bmatrix} = \begin{bmatrix} \mathbf{e} \\ \mathbf{h} \end{bmatrix} \quad (10.86)$$

where

$$\begin{aligned}
A_{mn} = & jk\eta \int_{C_m} \left\{ \iint \bar{B}_n(u', v') \frac{e^{-jkR}}{4\pi R} du' dv' \right\} \cdot d\bar{t} \\
& + \frac{\eta}{jk} \int_{C_m} \nabla \left\{ \iint [\nabla_s \cdot \bar{B}_n] \frac{e^{-jkR}}{4\pi R} du' dv' \right\} \cdot d\bar{t} \\
& + jk_d \eta_d \int_{C_m} \left\{ \iint \bar{B}_n(u', v') \frac{e^{-jk_d R}}{4\pi R} du' dv' \right\} \cdot d\bar{t} \\
& + \frac{\eta_d}{jk_d} \int_{C_m} \nabla \left\{ \iint [\nabla_s \cdot \bar{B}_n] \frac{e^{-jk_d R}}{4\pi R} du' dv' \right\} \cdot d\bar{t} \quad (10.87)
\end{aligned}$$

$$\begin{aligned}
B_{mn} = & - \int_{C_m} \left\{ \nabla \times \iint \bar{B}_n(u', v') \frac{e^{-jkR}}{4\pi R} du' dv' \right\}_{S^+} \cdot d\bar{t} \\
& - \int_{C_m} \left\{ \nabla \times \iint \bar{B}_n(u', v') \frac{e^{-jk_d R}}{4\pi R} du' dv' \right\}_{S^-} \cdot d\bar{t} \quad (10.88)
\end{aligned}$$

$$\begin{aligned}
C_{mn} = & \int_{C_m} \left\{ \nabla \times \iint \bar{B}_n(u', v') \frac{e^{-jkR}}{4\pi R} du' dv' \right\}_{S^+} \cdot d\bar{t} \\
& + \int_{C_m} \left\{ \nabla \times \iint \bar{B}_n(u', v') \frac{e^{-jk_d R}}{4\pi R} du' dv' \right\}_{S^-} \cdot d\bar{t} \quad (10.89)
\end{aligned}$$

$$\begin{aligned}
D_{mn} = & \frac{jk}{\eta} \int_{C_m} \left\{ \iint \bar{B}_n(u', v') \frac{e^{-jkR}}{4\pi R} du' dv' \right\} \cdot d\bar{t} \\
& + \frac{1}{jk\eta} \int_{C_m} \nabla \left\{ \iint [\nabla_s \cdot \bar{B}_n] \frac{e^{-jkR}}{4\pi R} du' dv' \right\} \cdot d\bar{t} \\
& + \frac{jk_d}{\eta_d} \int_{C_m} \left\{ \iint \bar{B}_n(u', v') \frac{e^{-jk_d R}}{4\pi R} du' dv' \right\} \cdot d\bar{t} \\
& + \frac{1}{jk_d \eta_d} \int_{C_m} \nabla \left\{ \iint [\nabla_s \cdot \bar{B}_n] \frac{e^{-jk_d R}}{4\pi R} du' dv' \right\} \cdot d\bar{t} \quad (10.90)
\end{aligned}$$

The entries of the right-hand side are

$$e_m = - \int_{C_m} \bar{E}^{\text{inc}} \cdot d\bar{t} \quad (10.91)$$

$$h_m = - \int_{C_m} \bar{H}^{\text{inc}} \cdot d\bar{t} \quad (10.92)$$

The double integrals in (10.86)–(10.90) denote integration over the entire scatterer surface; in actuality, these integrals collapse to the two cells in which the n th basis function is nonzero.

For efficient implementation, we consider some of the approximations introduced in Section 10.2 to simplify the matrix entries. Entries A_{mn} and D_{mn} can be simplified using

$$\int_{C_m} \nabla \Phi \cdot d\bar{t} = \Phi(u_j, v_j) - \Phi(u_i, v_i) \quad (10.93)$$

$$\int_{C_m} \bar{A} \cdot d\bar{t} \cong \bar{A} \cdot \Delta \bar{t}_{m1}|_{u_i, v_i} + \bar{A} \cdot \Delta \bar{t}_{m2}|_{u_j, v_j} \quad (10.94)$$

where, assuming that i and j are the two cells associated with edge m as depicted in Figure

10.10, $\Delta\bar{t}_{m1}$ denotes the vector from the centroid of cell i to the center of edge m and $\Delta\bar{t}_{m2}$ denotes the vector from the center of edge m to the centroid of cell j . Using (10.93) and (10.94), A_{mn} can be written entirely in terms of double integrals as

$$\begin{aligned}
 A_{mn} \cong & jk\eta \left\{ \Delta\bar{t}_{m1} \cdot \iint \bar{B}_n(u', v') \frac{e^{-jkR}}{4\pi R} du' dv' \Big|_{u_i, v_i} \right. \\
 & + \Delta\bar{t}_{m2} \cdot \iint \bar{B}_n(u', v') \frac{e^{-jkR}}{4\pi R} du' dv' \Big|_{u_j, v_j} \Big\} \\
 & + \frac{\eta}{jk} \left\{ \iint [\nabla_s \cdot \bar{B}_n] \frac{e^{-jkR}}{4\pi R} du' dv' \Big|_{u_j, v_j} \right. \\
 & - \iint [\nabla_s \cdot \bar{B}_n] \frac{e^{-jkR}}{4\pi R} du' dv' \Big|_{u_i, v_i} \Big\} \\
 & + jk_d\eta_d \left\{ \Delta\bar{t}_{m1} \cdot \iint \bar{B}_n(u', v') \frac{e^{-jk_d R}}{4\pi R} du' dv' \Big|_{u_i, v_i} \right. \\
 & + \Delta\bar{t}_{m2} \cdot \iint \bar{B}_n(u', v') \frac{e^{-jk_d R}}{4\pi R} du' dv' \Big|_{u_j, v_j} \Big\} \\
 & + \frac{\eta_d}{jk_d} \left\{ \iint [\nabla_s \cdot \bar{B}_n] \frac{e^{-jk_d R}}{4\pi R} du' dv' \Big|_{u_j, v_j} \right. \\
 & - \iint [\nabla_s \cdot \bar{B}_n] \frac{e^{-jk_d R}}{4\pi R} du' dv' \Big|_{u_i, v_i} \Big\}
 \end{aligned} \tag{10.95}$$

Because of the similarity between (10.87) and (10.90), an analogous expression for D_{mn} is immediately obtained. When source and observation regions coincide, the $1/R$ singularity may be extracted, integrated analytically, and added back to the numerically computed residual.

For the situation where the path C_m does not traverse either of the two source cells (the cells adjacent to edge n), B_{mn} may be simplified to

$$\begin{aligned}
 B_{mn} = & \int_{C_m} \left\{ \iint \bar{B}_n(u', v') \times \nabla \left(\frac{e^{-jkR}}{4\pi R} \right) du' dv' \right\}_{S^+} \cdot d\bar{t} \\
 & + \int_{C_m} \left\{ \iint \bar{B}_n(u', v') \times \nabla \left(\frac{e^{-jk_d R}}{4\pi R} \right) du' dv' \right\}_{S^-} \cdot d\bar{t} \\
 \cong & \iint \bar{B}_n(u', v') \times \nabla \left(\frac{e^{-jkR}}{4\pi R} \right) du' dv' \Big|_{u_i, v_i} \cdot \Delta\bar{t}_1 \\
 & + \iint \bar{B}_n(u', v') \times \nabla \left(\frac{e^{-jkR}}{4\pi R} \right) du' dv' \Big|_{u_j, v_j} \cdot \Delta\bar{t}_2 \\
 & + \iint \bar{B}_n(u', v') \times \nabla \left(\frac{e^{-jk_d R}}{4\pi R} \right) du' dv' \Big|_{u_i, v_i} \cdot \Delta\bar{t}_1 \\
 & + \iint \bar{B}_n(u', v') \times \nabla \left(\frac{e^{-jk_d R}}{4\pi R} \right) du' dv' \Big|_{u_j, v_j} \cdot \Delta\bar{t}_2
 \end{aligned} \tag{10.96}$$

For the case where the path C_m lies within a source cell, a limiting procedure may be used to obtain

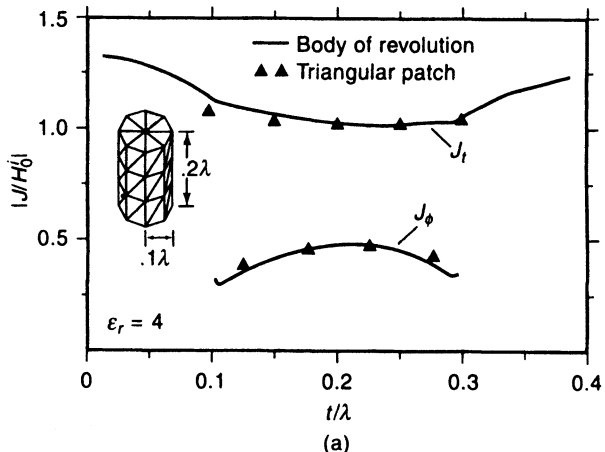
$$\int_{C_m^i} \left\{ \nabla \times \iint_{\text{cell } i} \bar{B}_n(u', v') \frac{e^{-jkR}}{4\pi R} du' dv' \right\}_{S^+} \cdot d\bar{t} = \int_{C_m^i} \frac{\bar{B}_n(u, v) \times \hat{n}}{2} \cdot d\bar{t} \quad (10.97)$$

where C_m^i denotes the part of path C_m within cell i . A similar limiting procedure produces

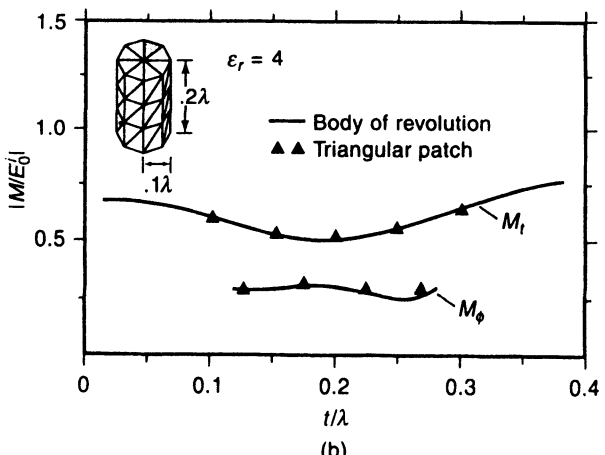
$$\int_{C_m^i} \left\{ \nabla \times \iint_{\text{cell } i} \bar{B}_n(u', v') \frac{e^{-jkR}}{4\pi R} du' dv' \right\}_{S^-} \cdot d\bar{t} = - \int_{C_m^i} \frac{\bar{B}_n(u, v) \times \hat{n}}{2} \cdot d\bar{t} \quad (10.98)$$

Equations (10.97) and (10.98) can be used to evaluate B_{mn} and C_{mn} when the source and observation regions coincide.

Other aspects of the CFIE implementation for homogeneous dielectric bodies such as the specific pointer arrays required within the scatterer model, the procedures used to eliminate redundant numerical calculations while constructing the matrix, and the details of the scattering cross section calculation are similar to those described in preceding sections of this chapter and will be left to the reader. To illustrate the approach, Figure 10.16 shows the surface currents associated with a finite dielectric cylinder produced by a triangular-cell



(a)



(b)

Figure 10.16 Current distribution on the surface of a finite dielectric cylinder due to an axially incident plane wave. The triangular-patch CN/LT results are compared to a body of revolution formulation. (a) Electric surface current. (b) Magnetic surface current. After [17]. ©1986 IEEE.

CFIE formulation similar to that outlined above [17]. The results exhibit good agreement with an alternative body-of-revolution approach.

10.8 RADIATION AND SCATTERING FROM THIN WIRES

The analysis of thin conducting wires is one of the most mature applications of computational electromagnetics, with hundreds of articles and a number of texts primarily devoted to this topic (see, e.g., [18, 19]). Yet wire modeling remains challenging, since often the parameters of interest such as antenna input impedance can be very sensitive to the detailed geometry of the feed region and resolution limitations govern the extent to which these regions can be modeled. In addition to antenna analysis, wire-grid models have been widely used to represent three-dimensional conducting scatterers. This section provides a brief overview of a typical thin-wire formulation based on the EFIE.

Consider a single wire having a circular cross section of radius a whose surface is described by local coordinates (s, Ψ) as illustrated in Figure 10.17. The principal assumptions of thin-wire analysis are that (1) circumferential currents around the wire are negligible and (2) the current density is not a function of Ψ . Under these assumptions, the surface current density $\bar{J}(s, \Psi)$ can be replaced by the total current

$$\hat{s}I(s) = 2\pi a \bar{J}(s, \Psi) \quad (10.99)$$

The mixed-potential form of the EFIE can be specialized to this situation to produce

$$E_s^{\text{inc}}(s) = j\omega\mu \int_s I(s')G(s, s') ds' - \frac{1}{j\omega\epsilon} \frac{d}{ds} \int_s \frac{dI}{ds'} G(s, s') ds' \quad (10.100)$$

where

$$G(s, s') = \frac{1}{2\pi a} \int_{\Psi'=0}^{2\pi} \frac{e^{-jkR}}{4\pi R} a d\Psi' \quad (10.101)$$

$$R = \sqrt{[x(s, 0) - x(s', \Psi')]^2 + [y(s, 0) - y(s', \Psi')]^2 + [z(s, 0) - z(s', \Psi')]^2} \quad (10.102)$$

and where $x(s, \Psi)$, $y(s, \Psi)$, and $z(s, \Psi)$ provide the coordinates of a point along the wire surface. The integrals in (10.100) extend over the length of the wire.

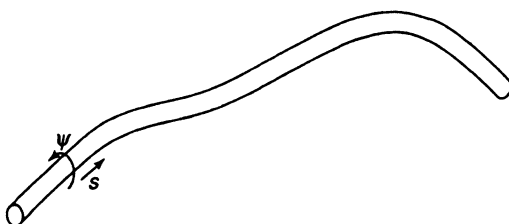


Figure 10.17 Thin-wire geometry.

Suppose that the wire is modeled by N straight, cylindrical segments (Figure 10.18) and the current $I(s)$ is represented by subsectional triangle basis functions (Figure 5.1)

$$I(s) \cong \sum_{n=1}^{N-1} I_n B_n(s) = \sum_{n=1}^{N-1} I_n t(s; s_{n-1}, s_n, s_{n+1}) \quad (10.103)$$

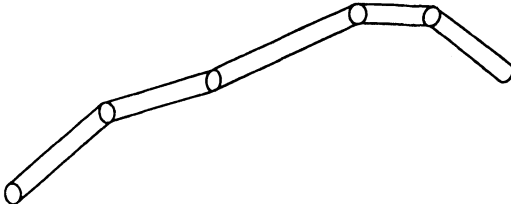


Figure 10.18 Model of thin wire consisting of straight cylindrical segments.

In other words, $I(s)$ is represented by a continuous, linear expansion. Assuming that the wire is hollow or that the endcap currents are negligible, $I(s)$ vanishes at the wire ends, and no basis functions are assigned to locations $n = 0$ and $n = N$.

The EFIE in (10.100) can be discretized using subsectional pulse testing functions

$$T_m(s) = p\{s; \frac{1}{2}(s_{m-1} + s_m), \frac{1}{2}(s_m + s_{m+1})\} \quad m = 1, 2, \dots, N - 1 \quad (10.104)$$

to produce the matrix equation $\mathbf{ZI} = \mathbf{E}^i$. The entries of \mathbf{I} are the coefficients in (10.103), while the entries of \mathbf{Z} are given by

$$\begin{aligned} Z_{mn} = & j\omega\mu \int_{(s_{m-1}+s_m)/2}^{(s_m+s_{m+1})/2} \int_{s_{n-1}}^{s_{n+1}} B_n(s') G(s, s') ds' ds \\ & + \frac{1}{j\omega\epsilon} \int_{s_{n-1}}^{s_{n+1}} \frac{dB_n}{ds'} G\left(\frac{s_{m-1} + s_m}{2}, s'\right) ds' \\ & - \frac{1}{j\omega\epsilon} \int_{s_{n-1}}^{s_{n+1}} \frac{dB_n}{ds'} G\left(\frac{s_m + s_{m+1}}{2}, s'\right) ds' \end{aligned} \quad (10.105)$$

where the pulse testing function in the scalar potential term is used to eliminate the derivative with respect to s . The expression

$$E_m^i = \int_{(s_{m-1}+s_m)/2}^{(s_m+s_{m+1})/2} E_s^{\text{inc}}(s) ds \quad (10.106)$$

provides the entries of the excitation vector \mathbf{E}^i .

If the incident field is a uniform plane wave, as in a scattering problem, the evaluation of (10.106) needs little elaboration. If the wire represents a radiating antenna, then one of a number of feed models can be employed as the source of E_s^{inc} . For example, a “magnetic frill” is often employed as a model for a wire fed by a coaxial transmission line through a ground plane (Chapter 1). Probably the most widely used model, however, is the so-called delta-gap feed, which consists of an idealized constant electric field in a small gap in the wire, scaled (like a Dirac delta function) so that the integral in (10.106) over the feed cell always has a constant value, regardless of how small the cell is. (The other cells receive no contribution from the feed.) The delta-gap feed can produce reasonable results if the cells are not too small; however, as the cell sizes shrink, the physical feed model changes and the resulting input impedance does not converge. A more realistic model is obtained by evaluating (by quadrature if necessary) the fields produced by the equivalent magnetic current density in the aperture of a small gap, where the finite gap size is maintained as the cells in the model are refined.

The most challenging aspect of the thin-wire formulation is the efficient and accurate evaluation of $G(s, s')$. Consider the evaluation of G when the observation point s resides on the surface of one cylindrical segment and the source point s' resides on another. The spherical angles (θ_p, ϕ_p) and (θ_q, ϕ_q) define the orientation of the two cylinders, and (x_p, y_p, z_p)

describes the location along the axis of the cylinder p at s while (x_q, y_q, z_q) denotes the location along the axis of cylinder q at s' (Figure 10.19). Without loss of generality, the observation point at $(s, 0)$ can be assigned the coordinates

$$x = x_p + a_p \cos \theta_p \cos \phi_p \quad (10.107)$$

$$y = y_p + a_p \cos \theta_p \sin \phi_p \quad (10.108)$$

$$z = z_p - a_p \sin \theta_p \quad (10.109)$$

while the source point at (s', Ψ') can be assigned

$$x' = x_q + a_q \cos \theta_q \cos \phi_q \cos \Psi' - a_q \sin \theta_q \sin \Psi' \quad (10.110)$$

$$y' = y_q + a_q \cos \theta_q \sin \phi_q \cos \Psi' + a_q \cos \phi_q \sin \Psi' \quad (10.111)$$

$$z' = z_q - a_q \sin \theta_q \cos \Psi' \quad (10.112)$$

Using these expressions within R in (10.102), $G(s, s')$ can be evaluated by quadrature to construct the off-diagonal entries of the matrix \mathbf{Z} .

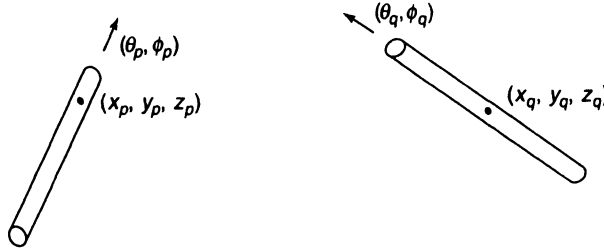


Figure 10.19 Coordinates and orientation parameters for the source and observer segments of the thin-wire model.

The diagonal matrix entries must be computed separately because of the singularity in G when $s = s'$. However, in that case Z_{mm} is identical to the matrix expressions previously developed for the hollow-cylinder example in Section 8.7 and can be found by specializing Equations (8.122)–(8.127) to the ϕ -invariant case.

Formulations similar to the above have been well documented in the literature, and representative results can be found in many publications. The triangle basis–pulse testing scheme is similar to the approach used in the commercial code MININEC [20], while other widely used discretizations include sinusoidal triangle basis and testing functions [21] and the three-term sinusoid basis function [22] (both of which are described in Chapter 5). Since the one-dimensional representation is easily realized, a wide variety of other basis functions have also been studied for thin-wire modeling [23].

Because of the complexity of $G(s, s')$, the numerical evaluation of (10.101) is usually modified to incorporate approximations that simplify the calculations. A number of accurate approximations are possible [18–24], although others that have been proposed are inaccurate. A widely used approximation is to replace (10.101) by the “thin-wire,” or “reduced,” kernel obtained by locating the observation point on the axis of the cylinder instead of the surface. For instance, when $p = q$, the integral is replaced by

$$\int_{\Psi'=0}^{2\pi} \frac{e^{-jkR}}{4\pi R} a d\Psi' \cong 2\pi a \frac{e^{-jk\sqrt{(s-s')^2+a^2}}}{4\pi \sqrt{(s-s')^2+a^2}} \quad (10.113)$$

This type of approximation eliminates the need to integrate over the variable Ψ' and removes the singularity from the kernel. Although (10.113) is a poor approximation and has been identified as the cause of irregular numerical results, the accuracy of Z_{mm} can be acceptable

if the cylindrical sections of the model have a length-to-radius ratio of at least 10 [25]. Actually, the results for currents and antenna impedance based on (10.113) have a much wider range of validity than one would expect from the accuracy of the approximation, apparently because the resulting system of equations is equivalent to the discrete system obtained from the so-called extended boundary condition formulation for the wire geometry [25, 26].

It is not necessary to make unwarranted approximations. Accurate approximations are well documented and, in fact, a highly accurate evaluation of G is possible and relatively efficient [27]. There are a number of other issues associated with wire antenna modeling that are beyond the scope of the present discussion. As mentioned above, the feed region geometry may require a level of resolution not possible with a particular formulation. Ideally, the geometrical features of the desired feed model should be incorporated into the formulation. Another application limited by resolution is the treatment of wire junctions. Several approaches have been proposed and include a model for junctions between wires of different radii [18, 22]. The use of a wire grid to represent the surface of a conducting scatterer is a powerful tool, but certain constraints must be placed on the wire dimensions to ensure an equivalence. Practical guidelines are available in the literature for assigning the wire radius and spacing in order to represent solid targets [18, 28].

10.9 SCATTERING FROM PLANAR PERIODIC GEOMETRIES

Figure 10.20 shows a doubly periodic planar structure consisting of a number of conducting patches. Structures of this type, known as *frequency-selective surfaces*, are used as filters, polarizers, and artificial dielectrics [8]. The analysis of doubly periodic scatterers is similar to the singly periodic case considered in Chapter 7, and this section provides a cursory overview of the planar three-dimensional case for completeness. Suppose that the unit cell is rectangular with dimensions $a \times b$, corresponding to the x and y directions. The currents induced by a uniform plane wave satisfy the Floquet condition

$$\bar{J}(x + ma, y + nb) = \bar{J}(x, y)e^{-jk_x^{\text{inc}}ma}e^{-jk_y^{\text{inc}}nb} \quad (10.114)$$

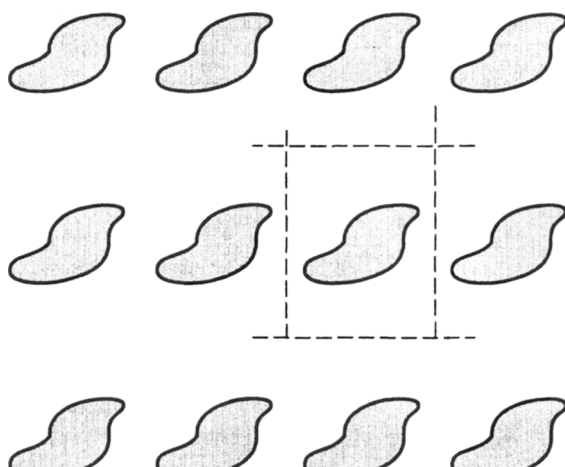


Figure 10.20 Portion of a doubly periodic frequency-selective surface showing the unit cell.

where k_x^{inc} and k_y^{inc} are the projection of the phase constants associated with the incident wave. In a situation where the conducting patches occupy less than half the area of the unit cell, it is convenient to employ an EFIE formulation using the equivalent electric current density on the conductors as the primary unknown. (If the patches occupy most of the unit cell, a formulation employing the tangential electric field in the aperture as the primary unknown would be more efficient.) The components of the EFIE for the periodic structure can be written as

$$E_x^{\text{inc}}(x, y) = -\hat{x} \cdot \frac{\nabla \nabla \cdot + k^2}{j\omega\epsilon_0} \iint \bar{J}(x', y') G_p(x - x', y - y') dx' dy' \quad (10.115)$$

$$E_y^{\text{inc}}(x, y) = -\hat{y} \cdot \frac{\nabla \nabla \cdot + k^2}{j\omega\epsilon_0} \iint \bar{J}(x', y') G_p(x - x', y - y') dx' dy' \quad (10.116)$$

where, using the Floquet condition, the periodic Green's function can be deduced to have the form

$$G_p(x, y) = \sum_{m=-\infty}^{\infty} \sum_{n=-\infty}^{\infty} \frac{e^{-jkR_{mn}}}{4\pi R_{mn}} e^{-jk_x^{\text{inc}}ma} e^{-jk_y^{\text{inc}}nb} \quad (10.117)$$

where

$$R_{mn} = \sqrt{(x - ma)^2 + (y - nb)^2} \quad (10.118)$$

Equations (10.115) and (10.116) are only valid for points (x, y) on the conducting patch.

Suppose that the conductor geometry is approximated by rectangular cells, as previously described for the aperiodic plate formulation (Figure 10.1). The method-of-moments analysis can be implemented in a manner almost identical to that for the individual conducting plate in Section 10.1 using rooftop basis functions for the current density

$$\bar{J}(x, y) \cong \hat{x} \sum_{p=1}^P j_{xp} B_{xp}(x, y) + \hat{y} \sum_{q=1}^Q j_{yq} B_{yq}(x, y) \quad (10.119)$$

and razor-blade testing functions to enforce the equations. The primary difference between the single plate and the periodic structure implementations is the need to accelerate the convergence of the periodic Green's function, since the terms in the summation in (10.117) only decay as $O(m^{-1})$ as $m \rightarrow \infty$ and $O(n^{-1})$ as $n \rightarrow \infty$. Problems P7.8 and P7.9 suggest the use of the Poisson sum transformation to produce the alternative summation

$$G_p(x, y) = \frac{1}{2ab} \sum_{m=-\infty}^{\infty} \sum_{n=-\infty}^{\infty} \frac{1}{j\beta z} e^{j2\pi f x} e^{j2\pi g y} \Bigg|_{f=m/a-k_x^{\text{inc}}/2\pi, g=n/b-k_y^{\text{inc}}/2\pi} \quad (10.120)$$

where

$$\beta_z = \begin{cases} \sqrt{k^2 - (2\pi f)^2 - (2\pi g)^2} & k^2 > (2\pi f)^2 + (2\pi g)^2 \\ -j\sqrt{(2\pi f)^2 + (2\pi g)^2 - k^2} & \text{otherwise} \end{cases} \quad (10.121)$$

Unfortunately, this summation also converges at an $O(m^{-1})$ and $O(n^{-1})$ rate.

Some acceleration can be provided by the basis and testing functions, as explained in Section 7.4, since the entries of the matrix equation have the convolutional form illustrated in Equations (10.20)–(10.23) [8]. However, a more effective approach can be based on

a three-dimensional extension of the error function transformation discussed for the two-dimensional case in Section 7.5 [29, 30].

Using the definition of the error function and the complementary error function in Equations (7.79) and (7.80), respectively, the Green's function in (10.120) can be divided into two parts according to

$$G_p(x, y) = G_1(x, y) + G_2(x, y) \quad (10.122)$$

where

$$G_1(x, y) = \frac{1}{2ab} \sum_{m=-\infty}^{\infty} \sum_{n=-\infty}^{\infty} \frac{\operatorname{erfc}(j\beta_z/2E)}{j\beta z} e^{j2\pi f_x} e^{j2\pi gy} \Bigg|_{f=m/a-k_x^{\text{inc}}/2\pi, g=n/b-k_y^{\text{inc}}/2\pi} \quad (10.123)$$

$$G_2(x, y) = \frac{1}{2ab} \sum_{m=-\infty}^{\infty} \sum_{n=-\infty}^{\infty} \frac{\operatorname{erf}(j\beta_z/2E)}{j\beta z} e^{j2\pi f_x} e^{j2\pi gy} \Bigg|_{f=m/a-k_x^{\text{inc}}/2\pi, g=n/b-k_y^{\text{inc}}/2\pi} \quad (10.124)$$

The summation for G_1 is exponentially convergent. Using the two-dimensional Poisson sum transformation, G_2 can be converted into an equivalent spatial domain summation

$$G_2(x, y) = \frac{1}{2\pi^{3/2}} \sum_{m=-\infty}^{\infty} \sum_{n=-\infty}^{\infty} e^{-jk_x^{\text{inc}}ma} e^{-jk_y^{\text{inc}}nb} \int_0^{1/2E} \frac{\exp(R_{mn}^2/4u^2 + k^2u^2)}{u^2} du \quad (10.125)$$

where R_{mn} is defined in (10.118). After a change of variables $w = 1/4u^2$, the integration can be performed analytically to produce

$$G_2(x, y) = \frac{1}{8\pi} \sum_{m=-\infty}^{\infty} \sum_{n=-\infty}^{\infty} \frac{e^{-jk_x^{\text{inc}}ma} e^{-jk_y^{\text{inc}}nb}}{R_{mn}} \times \left[\operatorname{erfc}\left(\frac{R_{mn}}{E} + \frac{jkE}{2}\right) e^{jkR_{mn}} + \operatorname{erfc}\left(\frac{R_{mn}}{E} - \frac{jkE}{2}\right) e^{-jkR_{mn}} \right] \quad (10.126)$$

which is also exponentially convergent. Therefore, the periodic Green's function can be obtained from the combination of (10.123) and (10.126). Additional details of the error function transformation and the more general Ewald transformation can be found in the literature [29–31].

The acceleration procedure permits a highly accurate evaluation of G_p , from which the entries of the method-of-moments matrix can be determined. The solution of the system of equations yields the basis function coefficients in (10.119) and subsequently reflection and transmission coefficients (Chapter 7). The literature contains a wide variety of numerical results for periodic surfaces and illustrates their applications [8, 32].

10.10 ANALYSIS OF MICROSTRIP STRUCTURES

Conducting patches on the surface of a grounded dielectric slab (“microstrip” patches) are widely used as antennas [33]. Their radiation and scattering properties can be determined by the numerical solution of an EFIE [6, 7, 34–38]. In order to limit the unknowns to the electric surface currents on the patch, the formulation must incorporate the Green's function for a horizontal electric point source on the surface of the grounded slab (Figure 10.21).

In this section, the appropriate Green's function is obtained using Fourier transform theory and a transmission line analogy.

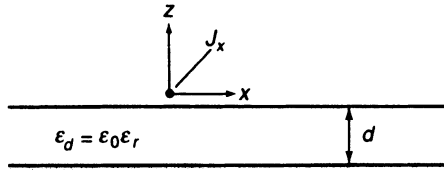


Figure 10.21 Point source on the surface of a grounded dielectric slab.

To obtain a Green's function involving a planar, layered geometry, it is convenient to work with Fourier transforms. The two-dimensional transform pair can be defined according to

$$\tilde{F}(k_x, k_y) = \int_{-\infty}^{\infty} \int_{-\infty}^{\infty} f(x, y) e^{-jk_x x} e^{-jk_y y} dx dy \quad (10.127)$$

$$f(x, y) = \frac{1}{(2\pi)^2} \int_{-\infty}^{\infty} \int_{-\infty}^{\infty} \tilde{F}(k_x, k_y) e^{jk_x x} e^{jk_y y} dk_x dk_y \quad (10.128)$$

(This is the identical transform used in Section 10.9 with $2\pi f$ replaced by k_x and $2\pi g$ replaced by k_y .) By applying the two-dimensional Fourier transform to the electric and magnetic fields, Maxwell's equations can be simplified to equations for the x - and y -field components as a function of the single variable z (and parameters k_x and k_y). Problem P10.14 reviews the development of the simplified equations. The one-dimensional equations are the same as those used to describe voltages and currents on transmission lines, and a transmission line analogy can be used to obtain the solutions [7, 39]. The Fourier transform can also be used to convert a point source at the origin (Figure 10.21) into a superposition of current sheets, according to

$$\begin{aligned} \tilde{J}(x, y, z) &= \hat{x} \delta(x) \delta(y) \delta(z) \\ &= \hat{x} \delta(z) \frac{1}{(2\pi)^2} \int_{-\infty}^{\infty} \int_{-\infty}^{\infty} e^{jk_x x} e^{jk_y y} dk_x dk_y \end{aligned} \quad (10.129)$$

In the transform domain, the appropriate transmission line equations can be solved individually for each current sheet, then superimposed via the inverse transform operation to produce the fields of the original point source in the spatial domain.

The equations obtained in Prob. P10.14 involve the coupled-field components E_x , E_y , H_x , and H_y . Additional simplification is possible by changing to polar coordinates and using [7]

$$k_x = k_\rho \cos \phi \quad (10.130)$$

$$k_y = k_\rho \sin \phi \quad (10.131)$$

where

$$k_\rho = \sqrt{k_x^2 + k_y^2} \quad (10.132)$$

and

$$\phi = \arctan \left(\frac{k_y}{k_x} \right) \quad (10.133)$$

The equations obtained in Prob. P10.14 decouple into two sets, the first given by

$$\frac{d\tilde{E}_\rho}{dz} - \frac{k^2 - k_\rho^2}{j\omega\epsilon} \tilde{H}_\phi = 0 \quad (10.134)$$

$$\frac{d\tilde{H}_\phi}{dz} + j\omega\epsilon \tilde{E}_\rho = 0 \quad (10.135)$$

and the second given by

$$\frac{d\tilde{E}_\phi}{dz} - j\omega\mu \tilde{H}_\rho = 0 \quad (10.136)$$

$$\frac{d\tilde{H}_\rho}{dz} + \frac{k^2 - k_\rho^2}{j\omega\mu} \tilde{E}_\phi = 0 \quad (10.137)$$

Each set of equations can be converted into an equivalent transmission line problem. Equations (10.134) and (10.135) can be rewritten using $V_1 = \tilde{E}_\rho$ and $I_1 = \tilde{H}_\phi$, to produce

$$\frac{dV_1}{dz} + j\beta Z_1 I_1 = 0 \quad (10.138)$$

$$\frac{dI_1}{dz} + j\frac{\beta}{Z_1} V_1 = 0 \quad (10.139)$$

where

$$\beta = \begin{cases} \sqrt{k^2 - k_\rho^2} & k^2 > k_\rho^2 \\ -j\sqrt{k_\rho^2 - k^2} & \text{otherwise} \end{cases} \quad (10.140)$$

and

$$Z_1 = \frac{\beta}{\omega\epsilon} \quad (10.141)$$

Equations (10.136) and (10.137) can be rewritten using $V_2 = -\tilde{E}_\phi$ and $I_2 = \tilde{H}_\rho$ to produce

$$\frac{dV_2}{dz} + j\beta Z_2 I_2 = 0 \quad (10.142)$$

$$\frac{dI_2}{dz} + j\frac{\beta}{Z_2} V_2 = 0 \quad (10.143)$$

where

$$Z_2 = \frac{\omega\mu}{\beta} \quad (10.144)$$

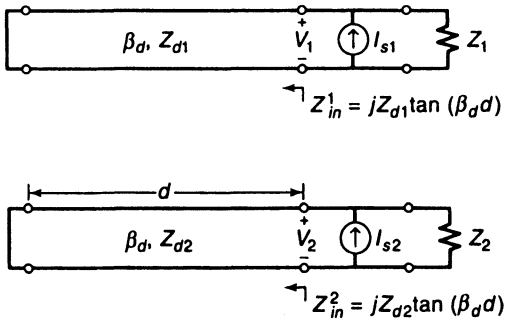
The transmission line systems described by these equations are uncoupled except by the source. An x -component current sheet such as (10.129) contributes a source

$$I_{s1} = -J_x \cos \phi \quad (10.145)$$

to the system in (10.138) and (10.139) and a source

$$I_{s2} = -J_x \sin \phi \quad (10.146)$$

to the system in (10.142) and (10.143). These current sources are located at $z = 0$ and are depicted in the transmission lines shown in Figure 10.22.



$$V_1 = \frac{Z_{in}^1 Z_1}{Z_{in}^1 + Z_1} I_{s1}, \quad V_2 = \frac{Z_{in}^2 Z_2}{Z_{in}^2 + Z_2} I_{s2}$$

Figure 10.22 Transmission line analogies.

From the transmission line analogy in Figure 10.22, we obtain

$$\tilde{E}_\rho(k_x, k_y) = V_1 = \frac{Z_1 Z_{d1}}{Z_{d1} - j Z_1 \cot(\beta_d d)} (-J_x \cos \phi) \quad (10.147)$$

$$-\tilde{E}_\phi(k_x, k_y) = V_2 = \frac{Z_2 Z_{d2}}{Z_{d2} - j Z_2 \cot(\beta_d d)} (-J_x \sin \phi) \quad (10.148)$$

where β_d is defined in (10.140) with k^2 replaced by $k^2 \epsilon_r$,

$$Z_{d1} = \frac{\beta_d}{\omega \epsilon_d} \quad (10.149)$$

$$Z_{d2} = \frac{\omega \mu}{\beta_d} \quad (10.150)$$

and $\epsilon_d = \epsilon \epsilon_r$ is the substrate permittivity. Consequently, the EFIE can be expressed in the form

$$E_x^{inc}(x, y) = -J_x * G_{xx} - J_y * G_{xy} \quad (10.151)$$

$$E_y^{inc}(x, y) = -J_x * G_{yx} - J_y * G_{yy} \quad (10.152)$$

where J_x and J_y are the components of the equivalent electric current density on the microstrip patch,

$$G_{xx}(x, y) = \frac{1}{(2\pi)^2} \frac{-1}{\omega \epsilon} \int_{-\infty}^{\infty} \int_{-\infty}^{\infty} \frac{k^2 D_1 - k_x^2 D_3}{D_1 D_2} e^{jk_x x} e^{jk_y y} dk_x dk_y \quad (10.153)$$

$$G_{xy}(x, y) = G_{yx}(x, y) = \frac{1}{(2\pi)^2} \frac{-1}{\omega \epsilon} \int_{-\infty}^{\infty} \int_{-\infty}^{\infty} \frac{-k_x k_y D_3}{D_1 D_2} e^{jk_x x} e^{jk_y y} dk_x dk_y \quad (10.154)$$

$$D_1 = \beta_d - j \beta \epsilon_r \cot(\beta_d d) \quad (10.155)$$

$$D_2 = \beta - j \beta_d \cot(\beta_d d) \quad (10.156)$$

$$D_3 = \beta_d - j \beta \cot(\beta_d d) \quad (10.157)$$

and G_{yy} is the same as G_{xx} with k_x and k_y exchanged [6]. The asterisk in (10.151) and (10.152) denotes two-dimensional convolution, and it is implied that the result of the con-

volution is to be evaluated at (x, y) . Equations (10.151) and (10.152) hold only on the location of the conducting patch. The incident electric field is evaluated in the presence of the substrate and ground plane, but in the absence of the patch.

For implementation purposes, it is sometimes convenient to convert the EFIE into the form of a mixed-potential integral equation [36, 37]

$$\bar{E}_{\tan}^{\text{inc}}(x, y) = \left(j\omega\mu\{\bar{J} * G_A\} + \nabla \left\{ \frac{\rho_s}{\epsilon} * G_\Phi \right\} \right)_{\tan} \quad (10.158)$$

where

$$\begin{aligned} G_A(x, y) &= \frac{1}{(2\pi)^2} \int_{-\infty}^{\infty} \int_{-\infty}^{\infty} \frac{-j}{D_2} e^{jk_x x} e^{jk_y y} dk_x dk_y \\ &= \frac{1}{2\pi} \int_0^{\infty} \frac{-jk_\rho J_0(k_\rho \rho)}{D_2} dk_\rho \end{aligned} \quad (10.159)$$

$$\begin{aligned} G_\Phi(x, y) &= \frac{1}{(2\pi)^2} \int_{-\infty}^{\infty} \int_{-\infty}^{\infty} \frac{-jD_3}{D_1 D_2} e^{jk_x x} e^{jk_y y} dk_x dk_y \\ &= \frac{1}{2\pi} \int_0^{\infty} \frac{-jk_\rho J_0(k_\rho \rho) D_3}{D_1 D_2} dk_\rho \end{aligned} \quad (10.160)$$

and

$$\rho_s = \frac{-\nabla_s \cdot \bar{J}}{j\omega} \quad (10.161)$$

The change of variables used to eliminate the double integrals is similar to that proposed in (10.130)–(10.133). The integrals in (10.159) and (10.160) are known as Sommerfeld integrals and are to be evaluated along a path of integration in the complex plane slightly above the real axis in order to avoid the singularities at zeros of the denominators. These integrals are further complicated by the growing oscillatory nature of the function $k_\rho J_0(k_\rho \rho)$ in the numerators. A special procedure known as the method of averages has been developed to combat the oscillation; other procedures can be applied to treat the integral in the vicinity of the surface wave poles [36, 37, 40, 41].

The numerical solution of the EFIE for microstrip proceeds as discussed in previous formulations and can be closely patterned after the treatment of conducting scatterers in free space (Sections 10.1 and 10.2). The essential difference is the evaluation of the Green's functions in (10.159) and (10.160).

Microstrip antenna analysis requires a model for the particular feed of interest (such as a probe feed or a microstrip line feed). In common with wire antennas, the input impedance is very sensitive to the specific feed region geometry, so the feed model must be tailored to the antenna under consideration. A current element can be used as a simple probe feed model if the substrate thickness is less than 0.02 wavelengths [35]. Microstrip line feeds that reside in the plane of the patch can be modeled as part of the integral equation analysis using additional basis functions to represent their currents. The representation can be terminated some distance from the patch where the currents become uniform [7, 40]. Other, more sophisticated methods for modeling the feeds have also been investigated [42, 43].

Arrays of microstrip patches can be analyzed by combining the ideas of this section with those of Section 10.9. The Fourier transform methodology is easily adapted to develop Green's functions for an infinite periodic array on a dielectric substrate. We refer the reader

to the literature for a detailed discussion of the treatment of antenna arrays [6, 43]. Green's functions for other multilayered devices can be developed in a similar manner [38, 39].

10.11 A BRIEF SURVEY OF VOLUME INTEGRAL FORMULATIONS FOR HETEROGENEOUS DIELECTRIC BODIES

To close this chapter, we briefly consider the analysis of three-dimensional heterogeneous scatterers using volume integral equations. Volume discretizations require numerous unknowns and are quite limited in the three-dimensional case. While largely superseded by the three-dimensional differential equation formulations (Chapters 11 and 12), volume integral methods may be preferred in situations involving electrically small structures in the vicinity of other scatterers being analyzed with integral equations or in situations where a thin heterogeneous structure is not practical for analysis using differential equation approaches. They also may be useful for validating differential equation formulations.

Suppose a three-dimensional dielectric scatterer can be characterized by a relative permittivity function $\epsilon_r(x, y, z)$. Using the volumetric equivalence principle (Chapter 1), the dielectric material may be replaced by an equivalent electric current density

$$\bar{J}(x, y, z) = j\omega\epsilon_0[\epsilon_r(x, y, z) - 1]\bar{E}(x, y, z) \quad (10.162)$$

radiating in free space. An electric field integral equation for the unknown current is

$$\bar{E}^{\text{inc}} = \bar{E} - \frac{\nabla \nabla \cdot + k^2}{j\omega\epsilon_0} \bar{A} \quad (10.163)$$

where

$$\bar{A}(x, y, z) = \iiint \bar{J}(x', y', z') \frac{e^{-jkR}}{4\pi R} dx' dy' dz' \quad (10.164)$$

and

$$R = \sqrt{(x - x')^2 + (y - y')^2 + (z - z')^2} \quad (10.165)$$

Equation (10.163) is valid both inside and outside the original scatterer but is imposed throughout the interior to find the equivalent current density.

A number of different approaches have been proposed for discretizing Equation (10.163). The most widely used procedure employs a cubical-cell model for the scatterer, a pulse basis expansion for the current \bar{J} or the electric field \bar{E} , and Dirac delta testing functions [44]. Unfortunately, in common with the two-dimensional case presented in Section 2.6, a cubical-cell pulse basis discretization proves unstable as the relative permittivity increases in magnitude [45–47]. However, since the approach has been widely used, we summarize it below.

Suppose that the three-dimensional scatterer is divided into N homogeneous cells that are approximately cubical and the polarization current density is represented by the superposition of $3N$ subsectional pulse basis functions

$$\bar{J}(x, y, z) \cong \sum_{n=1}^N (\hat{x}j_{xn} + \hat{y}j_{yn} + \hat{z}j_{zn}) p_n(x, y, z) \quad (10.166)$$

where

$$p_n(x, y, z) = \begin{cases} 1 & \text{if } (x, y, z) \in \text{cell } n \\ 0 & \text{otherwise} \end{cases} \quad (10.167)$$

Equation (10.163) may be separated into components and enforced at the center of each cell to yield a $3N \times 3N$ system

$$\begin{bmatrix} \mathbf{G}^{xx} & \mathbf{G}^{xy} & \mathbf{G}^{xz} \\ \mathbf{G}^{yx} & \mathbf{G}^{yy} & \mathbf{G}^{yz} \\ \mathbf{G}^{zx} & \mathbf{G}^{zy} & \mathbf{G}^{zz} \end{bmatrix} \begin{bmatrix} \mathbf{j}_x \\ \mathbf{j}_y \\ \mathbf{j}_z \end{bmatrix} = \begin{bmatrix} \mathbf{E}_x^{\text{inc}} \\ \mathbf{E}_y^{\text{inc}} \\ \mathbf{E}_z^{\text{inc}} \end{bmatrix} \quad (10.168)$$

with off-diagonal entries

$$G_{mn}^{uv} = \frac{-1}{j\omega\epsilon_0} \frac{\partial^2 g_n}{\partial u \partial v} \Big|_{(x=x_m, y=y_m, z=z_m)} \quad m \neq n \quad u \neq v \quad (10.169)$$

$$G_{mn}^{uu} = \frac{-1}{j\omega\epsilon_0} \left(\frac{\partial^2}{\partial u^2} + k^2 \right) g_n \Big|_{(x=x_m, y=y_m, z=z_m)} \quad m \neq n \quad (10.170)$$

and

$$G_{mm}^{uv} = 0 \quad u \neq v \quad (10.171)$$

where u and v represent x , y , or z , and

$$g_n(x, y, z) = \iiint_{\text{cell } n} \frac{e^{-jkR}}{4\pi R} dx' dy' dz' \quad (10.172)$$

Assuming that each cell can be approximated by a sphere (so that cell m has radius a_m), the diagonal entries may be evaluated approximately to produce (Prob. P1.15)

$$G_{mm}^{uu} \cong \frac{1}{j\omega\epsilon_0(\epsilon_r - 1)} + \frac{1}{j\omega\epsilon_0} \left[1 - \frac{2}{3} e^{-jka_m} (1 + jka_m) \right] \quad (10.173)$$

The remaining integrands in (10.169) and (10.170) are nonsingular and can be evaluated by numerical quadrature. We leave the details of the necessary calculations to the reader.

The above formulation is similar in many respects to the approach presented in Section 2.6 for TE-wave scattering from infinite dielectric cylinders. Section 2.6 demonstrated that the pulse basis discretization of the EFIE did not work well for cylinders having large values of the relative permittivity. Similar instabilities occur in the three-dimensional case [45–47] and limit the application of this particular formulation to relatively low values of ϵ_r . Because of these limitations, several alternative formulations have been proposed. One such procedure uses cubical cells to discretize the EFIE but places the match points on cell faces instead of cell centers [47]. By retaining the cubical cell models, the approach of [47] is able to exploit perturbed Toeplitz symmetries within a CG-FFT solution (Section 4.12), which is advantageous since the matrix order grows quickly with scatterer size. [The matrix has order $3N$, where N is the number of cells; to maintain accuracy, the cell density should be at least 1000 per cubic dielectric wavelength.]

Volume formulations with more flexible cell shapes have also been proposed. One approach employs the EFIE with piecewise linear basis functions defined on polyhedral cells [48]. The approach of Schaubert, Wilton, and Glisson uses a divergence-conforming CN/LT function defined on tetrahedral cells to discretize the EFIE [49]. Both of these

approaches attempt to use higher order basis functions to better represent the equivalent charge distribution. Parametric basis functions, defined on curved cells, may provide a better model [50]. The MFIE, which may be less sensitive to charge modeling, has also been studied for scattering from three-dimensional dielectric bodies modeled with tetrahedral cells [51]. By explicitly incorporating the surface charge density into the formulation, it is possible to convert volume integral equations into volume–surface equations, which separate the current and charge densities and may make it easier to properly model these quantities [52, 53].

Since all volume integral equation formulations suffer from a rapid growth of the associated computational complexity with increasing scatterer size, the application of these techniques in three-dimensions has been extremely limited. It appears that differential equation formulations that produce sparse matrices are more practical when three-dimensional volume discretizations are required, and Chapter 11 considers that type of formulation.

10.12 SUMMARY

The numerical solution of several types of integral equations have been considered for three-dimensional scatterers and antennas. Approaches were developed for conducting and homogeneous bodies of general shape using subsectional vector basis functions. The treatment of wire structures was also briefly reviewed. To illustrate the use of a variety of three-dimensional Green's functions, a planar frequency-selective surface formulation was presented, and the Green's functions for a microstrip patch on a grounded substrate were developed using a transmission line analogy. Finally, volume integral equations for modeling three-dimensional heterogeneous bodies were summarized.

REFERENCES

- [1] A. W. Glisson and D. R. Wilton, "Simple and efficient numerical methods for problems of electromagnetic radiation and scattering from surfaces," *IEEE Trans. Antennas Propagat.*, vol. AP-28, pp. 593–603, Sept. 1980.
- [2] H. Akaike, "Block-Toeplitz matrix inversion," *SIAM J. Appl. Math.*, vol. 24, pp. 234–241, Mar. 1973.
- [3] M. Hurst and R. Mittra, "Scattering center analysis for radar cross section modification," Electromagnetic Communication Laboratory Technical Report 84-12, UILU-ENG-84-2551, University of Illinois, Urbana, July 1984.
- [4] K. R. Aberegg, A. Taguchi, and A. F. Peterson, "Application of higher-order vector basis functions to surface integral formulations," *Radio Sci.*, vol. 31, pp. 1207–1213, 1996.
- [5] D. R. Wilton and S. Govind, "Incorporation of edge condition in moment method solutions," *IEEE Trans. Antennas Propagat.*, vol. AP-25, pp. 845–850, Nov. 1977.
- [6] S. M. Wright, "Efficient analysis of infinite microstrip arrays on electrically thick substrates," Ph.D. dissertation, University of Illinois, Urbana, 1984.
- [7] D. R. Tanner, "Numerical methods for the electromagnetic modeling of microstrip antennas and feed systems," Ph.D. dissertation, University of Illinois, Urbana, 1988.

- [8] R. Mittra, C.-H. Chan, and T. Cwik, "Techniques for analyzing frequency selective surfaces—a review," *Proc. IEEE*, vol. 76, pp. 1593–1615, Dec. 1988.
- [9] S. M. Rao, D. R. Wilton, and A. W. Glisson, "Electromagnetic scattering by surfaces of arbitrary shape," *IEEE Trans. Antennas Propagat.*, vol. AP-30, pp. 409–418, May 1982.
- [10] S. Caorsi, D. Moreno, and F. Sidoti, "Theoretical and numerical treatment of surface integrals involving the free-space Green's function," *IEEE Trans. Antennas Propagat.*, vol. 41, pp. 1296–1301, Sept. 1993.
- [11] R. D. Graglia, "On the numerical integration of the linear shape functions times the 3-D Green's function or its gradient on a plane triangle," *IEEE Trans. Antennas Propagat.*, vol. 41, pp. 1448–1455, Oct. 1993.
- [12] D. R. Wilton, "Review of current status and trends in the use of integral equations in computational electromagnetics," *Electromagnetics*, vol. 12, pp. 287–341, 1992.
- [13] D. R. Wilton, "Topological considerations in surface patch modeling," *Abstracts of the 1981 URSI Radio Science Meeting*, Boulder, CO, p. 9, Jan. 1981.
- [14] D. R. Wilton and A. W. Glisson, "On improving the stability of the electric field integral equation at low frequencies," *Abstracts of the 1981 URSI Radio Science Meeting*, Los Angeles, CA, p. 24, June 1981.
- [15] J. R. Mautz and R. F. Harrington, "An E-field solution for a conducting surface small or comparable to the wavelength," *IEEE Trans. Antennas Propagat.*, vol. AP-32, pp. 330–339, Apr. 1984.
- [16] E. Arvas, R. F. Harrington, and J. R. Mautz, "Radiation and scattering from electrically small conducting bodies of arbitrary shape," *IEEE Trans. Antennas Propagat.*, vol. AP-34, pp. 66–77, Jan. 1986.
- [17] K. Umashankar, A. Tafove, and S. M. Rao, "Electromagnetic scattering by arbitrary shaped three-dimensional homogeneous lossy dielectric objects," *IEEE Trans. Antennas Propagat.*, vol. AP-34, pp. 758–766, June 1986.
- [18] J. Moore and R. Pizer, eds., *Moment Methods in Electromagnetics*, Letchworth: Research Studies Press, 1984.
- [19] B. D. Popovic, M. B. Dragovic, and A. R. Djordjevic, *Analysis and Synthesis of Wire Antennas*, New York: Wiley, 1982.
- [20] S. T. Li, J. C. Logan, J. W. Rockway, and D. W. S. Tam, *The MININEC System: Microcomputer Analysis of Wire Antennas*, Boston: Artech House, 1988.
- [21] J. H. Richmond, "Radiation and scattering by thin-wire structures in the complex frequency domain," in *Computational Electromagnetics*, eds. E. K. Miller, L. Medgyesi-Mitschang, and E. H. Newman, New York: IEEE Press, 1992.
- [22] G. J. Burke and A. J. Poggio, *Numerical Electromagnetics Code (NEC)—Method of Moments*, Technical Document 116, Naval Ocean System Center, San Diego, Jan. 1981.
- [23] G. A. Thiele, "Wire antennas," in *Computer Techniques for Electromagnetics*, ed. R. Mittra, New York: Pergamon, 1973.
- [24] A. J. Poggio, "Numerical solutions of integral equations of dipoles and slot antennas including active and passive loading," Ph.D. dissertation, University of Illinois, Urbana, 1969.

- [25] A. F. Peterson, "Difficulties encountered when attempting to validate thin-wire formulations for linear dipole antennas," *Appl. Computat. Electromagnet. Soc. (ACES) J.*, vol. 4, Special Issue on Electromagnetics Computer Code Validation, pp. 25–40, 1989.
- [26] C. D. Taylor and D. R. Wilton, "The extended boundary condition solution of the dipole antenna of revolution," *IEEE Trans. Antennas Propagat.*, vol. AP-20, pp. 772–776, Nov. 1972.
- [27] D. H. Werner, J. A. Huffman, and P. L. Werner, "Techniques for evaluating the uniform current vector potential at the isolated singularity of the cylindrical wire kernel," *IEEE Trans. Antennas Propagat.*, vol. 42, pp. 1549–1553, Nov. 1994.
- [28] A. C. Ludwig, "Wire grid modeling of surfaces," *IEEE Trans. Antennas Propagat.*, vol. AP-35, pp. 1045–1048, Sept. 1987.
- [29] K. E. Jordan, G. R. Richter, and P. Sheng, "An efficient numerical evaluation of the Green's function for the Helmholtz operator on periodic structures," *J. Comp. Phys.*, vol. 63, pp. 222–235, 1986.
- [30] A. W. Mathis and A. F. Peterson, "A comparison of acceleration procedures for the two-dimensional periodic Green's function," *IEEE Trans. Antennas Propagat.*, vol. 44, pp. 567–571, Apr. 1996.
- [31] E. Cohen, "An Ewald transformation of frequency-domain integral formulations," *Electromagnetics*, vol. 15, pp. 427–439, 1995.
- [32] R. S. Zich, ed., "Special issue on frequency selective surfaces," *Electromagnetics*, vol. 5, 1985.
- [33] D. M. Pozar and D. H. Schaubert, eds., *Microstrip Antennas*, New York: IEEE Press, 1995.
- [34] M. C. Bailey and M. D. Deshpande, "Integral equation formulation of microstrip antennas," *IEEE Trans. Antennas Propagat.*, vol. AP-30, pp. 615–656, July 1982.
- [35] D. M. Pozar, "Input impedance and mutual coupling of rectangular microstrip antennas," *IEEE Trans. Antennas Propagat.*, vol. AP-30, pp. 1191–1196, Nov. 1982.
- [36] J. R. Mosig and F. E. Gardiol, "Analytical and numerical techniques in the Green's function treatment of microstrip antennas and scatterers," *IEE Proc., Part H*, vol. 130, pp. 175–182, 1983.
- [37] J. R. Mosig, "Arbitrarily shaped microstrip structures and their analysis with a mixed potential integral equation," *IEEE Trans. Microwave Theory Tech.*, vol. 36, pp. 314–323, Feb. 1988.
- [38] V. W. Hansen, *Numerical Solution of Antennas in Layered Media*, Taunton: Research Studies Press, 1989.
- [39] A. K. Bhattacharyya, *Electromagnetic Fields in Multilayered Structures*, Boston: Artech House, 1994.
- [40] J. R. Mosig, "Integral equation technique," in *Numerical Techniques for Microwave and Millimeter-Wave Passive Structures*, ed. T. Itoh, New York: Wiley, 1989.
- [41] L. T. Hildebrand and D. A. McNamara, "A guide to implementational aspects of the spatial-domain integral equation analysis of microstrip antennas," *ACES J.*, vol. 10, pp. 40–51, Mar. 1995.
- [42] M. Davidovitz, "Feed analysis for microstrip antennas," Ph.D. dissertation, University of Illinois, Urbana, 1985.

- [43] J. T. Aberle and D. M. Pozar, "Analysis of infinite arrays of probe-fed rectangular microstrip patches using a rigorous feed model," *IEE Proc., Part H*, vol. 136, pp. 110–119, 1989.
- [44] D. E. Livesay and K. M. Chen, "Electromagnetic fields induced inside arbitrarily shaped biological bodies," *IEEE Trans. Microwave Theory Tech.*, vol. MTT-22, pp. 1273–1280, Dec. 1974.
- [45] H. Massoudi, C. H. Durney, and M. F. Iskander, "Limitations of the cubical block model of man in calculating SAR distributions," *IEEE Trans. Microwave Theory Tech.*, vol. MTT-32, pp. 746–751, Aug. 1984.
- [46] M. J. Hagmann and R. L. Levin, "Criteria for accurate usage of block models," *J. Microwave Power*, vol. 22, pp. 19–27, January 1987.
- [47] C.-C. Su, "The three-dimensional algorithm of solving the electric-field integral equation using face-centered node points, conjugate gradient method, and FFT," *IEEE Trans. Microwave Theory Tech.*, vol. 41, pp. 510–515, Mar. 1993.
- [48] C. T. Tsai, H. Massoudi, C. H. Durney, and M. F. Iskander, "A procedure for calculating fields inside arbitrarily shaped, inhomogeneous dielectric bodies using linear basis functions with the moment method," *IEEE Trans. Microwave Theory Tech.*, vol. MTT-34, pp. 1131–1139, Nov. 1986.
- [49] D. H. Schaubert, D. R. Wilton, and A. W. Glisson, "A tetrahedral modeling method for electromagnetic scattering by arbitrarily shaped inhomogeneous dielectric bodies," *IEEE Trans. Antennas Propagat.*, vol. AP-32, pp. 77–85, Jan. 1984.
- [50] R. D. Graglia, P. L. E. Uslenghi, and R. S. Zich, "Moment method with isoparametric elements for three-dimensional anisotropic scatterers," *Proc. IEEE*, vol. 77, pp. 750–760, May 1989.
- [51] A. F. Peterson, "A magnetic field integral equation formulation for electromagnetic scattering from inhomogeneous 3D dielectric bodies," *Proceedings of the Fifth Annual Review of Progress in Applied Computational Electromagnetics*, Monterey, CA, pp. 387–403, Mar. 1989.
- [52] J. L. Volakis, "Alternative field representations and integral equations for modeling inhomogeneous dielectrics," *IEEE Trans. Microwave Theory Tech.*, vol. 40, pp. 604–608, Mar. 1992.
- [53] A. D. Yaghjian and R. W. Wang, "Electric- and magnetic-field volume-surface integral equations for 3-D inhomogeneous scatterers," *Abstracts of the 1994 URSI Radio Science Meeting*, Seattle, WA, p. 15, June 1994.

PROBLEMS

- P10.1** Using the aperture formulation in Chapter 1, Section 1.10, for guidance, modify the conducting-plate approach of Section 10.1 to obtain a method-of-moments equation for scattering from an aperture in an infinite p.e.c. plane. Treat the equivalent magnetic current density in the aperture as the primary unknown and use CN/LT basis functions on rectangular cells and razor-blade testing functions to discretize the integral equation. Describe in detail how the entries of the matrix equation (10.11) must be modified to convert the plate formulation into an aperture formulation.
- P10.2** Modify the flat-plate formulation in Section 10.1 in order to use rectangular-cell CN/LT functions for both expansion and testing (Galerkin's method). Use convolution properties to express all of the necessary matrix entries in terms of two-dimensional integrals.

Provide expressions for the new matrix entries in terms of pulse, triangle, quadratic, and cubic spline functions (Chapter 5).

- P10.3** Under what conditions is the matrix in (10.11), obtained using rectangular-cell CN/LT basis functions and razor-blade testing functions, symmetric across its main diagonal? Is the matrix produced in Prob. P10.2 with Galerkin's method always symmetric?
- P10.4** The p.e.c. plate formulation of Section 10.1 can be extended in order to model material plates that satisfy the resistive shell boundary condition

$$\bar{E} = R \bar{J},$$

where R is defined in Prob. P2.36. Describe the modifications to the entries of (10.11) needed to incorporate this boundary condition.

- P10.5** The CN/LT basis, razor-blade testing formulation from Section 10.1 involves only two fundamentally different expressions for the entries of the method-of-moments system, Equations (10.29) and (10.30). By studying the LN/QT basis functions introduced at the end of Section 10.1, determine how many different expressions arise in an LN/QT basis/razor-blade testing scheme for flat conducting plates discretized into uniform rectangular cells.
- P10.6** Equation (10.33) is an expression for the integral of $1/R$ over a rectangular domain. Provide a similar expression for a triangular domain, with the observation point (x, y) arbitrarily located within the triangle.
- P10.7** (a) A scatterer with top-to-bottom symmetry illuminated by a source with the same symmetry enables a 50% reduction in the required number of unknowns. Describe the process of constructing the method-of-moments matrix in order to exploit the symmetry.
(b) Suppose the scatterer in part (a) is symmetric but the illumination is not. Can the order of the method-of-moments matrix still be reduced by exploiting symmetry? What additional price must be paid in this case?
- P10.8** Section 10.3 presents an MFIE formulation using CN/LT basis functions. A simpler approach similar to that used in [22] to model closed conducting bodies can be obtained using pulse basis functions and Dirac delta testing functions to discretize the three-dimensional MFIE. Suppose the scatterer is represented by triangular patches, so that the outward normal vector to the n th patch is

$$\hat{n}_n = \sin \theta_n \cos \phi_n \hat{x} + \sin \theta_n \sin \phi_n \hat{y} + \cos \theta_n \hat{z}$$

where (θ_n, ϕ_n) denote conventional spherical coordinate angles. On each cell, the current density is decomposed into two orthogonal components J_u and J_v , where

$$\hat{u}_n = -\sin \phi_n \hat{x} + \cos \phi_n \hat{y}$$

$$\hat{v}_n = \hat{n}_n \times \hat{u}_n = -\cos \theta_n \cos \phi_n \hat{x} - \cos \theta_n \sin \phi_n \hat{y} + \sin \theta_n \hat{z}$$

Suppose that pulse basis functions are used to represent \bar{J} according to

$$\bar{J}(u, v) \cong \sum_{n=1}^N (\hat{u}_n j_{un} + \hat{v}_n j_{vn}) p_n(u, v)$$

where

$$p_n(u, v) = \begin{cases} 1 & \text{if } (u, v) \in \text{cell } n \\ 0 & \text{otherwise} \end{cases}$$

and Dirac delta testing functions are used to enforce the \hat{u} - and \hat{v} -components of the

MFIE

$$\hat{n} \times \bar{H}^{\text{inc}} = \bar{J}(u, v) - \hat{n} \times (\nabla \times \bar{A})_{S^+}$$

where

$$\bar{A}(x, y, z) = \iint \bar{J}(u', v') \frac{e^{-jkR}}{4\pi R} du' dv'$$

and where R is the distance from the source point (u', v') to the observation point (x, y, z) , also located on the surface. Show that the entries of the method-of-moments system

$$\begin{bmatrix} \mathbf{A}^{uu} & \mathbf{A}^{uv} \\ \mathbf{A}^{vu} & \mathbf{A}^{vv} \end{bmatrix} \begin{bmatrix} \mathbf{j}_u \\ \mathbf{j}_v \end{bmatrix} = \begin{bmatrix} \mathbf{H}_u^{\text{inc}} \\ \mathbf{H}_v^{\text{inc}} \end{bmatrix}$$

are given by

$$\begin{aligned} A_{mn}^{uu} &= \cos \theta_m \cos(\phi_m - \phi_n) \frac{\partial g_n}{\partial z} \\ &\quad + \sin \theta_m \left(\sin \phi_n \frac{\partial g_n}{\partial y} + \cos \phi_n \frac{\partial g_n}{\partial x} \right) \quad m \neq n \\ A_{mn}^{uv} &= \cos \theta_m \cos \theta_n \sin(\phi_m - \phi_n) \frac{\partial g_n}{\partial z} \\ &\quad - \cos \theta_m \sin \theta_n \left(\cos \phi_m \frac{\partial g_n}{\partial y} - \sin \phi_m \frac{\partial g_n}{\partial x} \right) \\ &\quad + \sin \theta_m \cos \theta_n \left(\cos \phi_n \frac{\partial g_n}{\partial y} - \sin \phi_n \frac{\partial g_n}{\partial x} \right) \quad m \neq n \\ A_{mn}^{vu} &= -\sin(\phi_m - \phi_n) \frac{\partial g_n}{\partial z} \quad m \neq n \\ A_{mn}^{vv} &= \sin \theta_n \left(\sin \phi_m \frac{\partial g_n}{\partial y} + \cos \phi_m \frac{\partial g_n}{\partial x} \right) \\ &\quad + \cos \theta_n \cos(\phi_m - \phi_n) \frac{\partial g_n}{\partial z} \quad m \neq n \\ A_{mm}^{uu} &= A_{mm}^{vv} = \frac{1}{2} \end{aligned}$$

and

$$A_{mm}^{uv} = A_{mm}^{vu} = 0$$

where

$$g_n(x, y, z) = \iint_{\text{patch } n} \frac{e^{-jkR}}{4\pi R} du' dv'$$

[Hint: First show that the scattered magnetic field at patch m can be written in the form

$$\begin{aligned} \hat{n}_m \times \bar{H}^s &= \hat{u}_m (\cos \theta_m \cos \phi_m H_x^s + \cos \theta_m \sin \phi_m H_y^s - \sin \theta_m H_z^s) \\ &\quad + \hat{v}_m (-\sin \phi_m H_x^s + \cos \phi_m H_y^s) \end{aligned}$$

Then, combine this result with the expressions

$$\begin{aligned} H_x^s &= \sin \theta_n j_{vn} \frac{\partial g_n}{\partial y} - (\cos \phi_n j_{un} - \cos \theta_n \sin \phi_n j_{vn}) \frac{\partial g_n}{\partial z} \\ H_y^s &= -(\sin \phi_n j_{un} + \cos \theta_n \cos \phi_n j_{vn}) \frac{\partial g_n}{\partial z} - \sin \theta_n j_{vn} \frac{\partial g_n}{\partial x} \\ H_z^s &= (\cos \phi_n j_{un} - \cos \theta_n \sin \phi_n j_{vn}) \frac{\partial g_n}{\partial x} \\ &\quad + (\sin \phi_n j_{un} + \cos \theta_n \cos \phi_n j_{vn}) \frac{\partial g_n}{\partial y} \end{aligned}$$

to complete the derivation.] Finally, provide a brief discussion of the numerical implementation of this approach.

- P10.9** An alternate CFIE for homogeneous dielectric scatterers can be obtained by constructing a linear combination of the exterior EFIE and MFIE and a linear combination of the interior EFIE and MFIE. How does such a formulation differ from Equations (10.82) and (10.83)?
- P10.10** Verify the coordinate transformation used in (10.107)–(10.112).
- P10.11** Suppose the frequency-selective surface (FSS) formulation of Section 10.9 is implemented using rectangular-cell CN/LT basis functions and razor-blade testing functions with uniform cell sizes (as in the aperiodic plate formulation of Section 10.1). Suppose further that the only acceleration procedure employed is that obtained by combining the Fourier transform of the basis and testing functions with G_p in (10.120). Provide explicit expressions for the matrix entries, and identify the rate of convergence of each summation.
- P10.12** Recast the conducting patch FSS formulation in Section 10.9 in order to treat a doubly periodic array of apertures using the equivalent magnetic current density in the aperture of the unit cell as the primary unknown. Provide the new integral equation in a form similar to (10.115) and (10.116) in terms of the periodic Green's function G_p defined in (10.117).
- P10.13** Using the exponentially convergent summations in (10.123) and (10.126), provide expressions for the matrix entries associated with the conducting patch FSS formulation using rectangular-cell CN/LT basis functions and razor-blade testing functions.
- P10.14** After decomposing the fields into longitudinal and transverse parts,

$$\begin{aligned} \bar{E} &= \hat{z} E_z + \bar{E}_t \\ \bar{H} &= \hat{z} H_z + \bar{H}_t \end{aligned}$$

Maxwell's curl equations for a uniform medium with sources (\bar{J}, \bar{K}) can be rewritten in the form

$$\begin{aligned} -\nabla_t \cdot (\hat{z} \times \bar{E}_t) &= -j\omega\mu H_z - K_z \\ -\nabla_t \cdot (\hat{z} \times \bar{H}_t) &= j\omega\epsilon E_z + J_z \\ -\frac{\partial \bar{E}_t}{\partial z} + \nabla_t E_z &= -j\omega\mu(\hat{z} \times \bar{H}_t) - \hat{z} \times \bar{K}_t \\ -\frac{\partial \bar{H}_t}{\partial z} + \nabla_t H_z &= j\omega\epsilon(\hat{z} \times \bar{E}_t) + \hat{z} \times \bar{J}_t \end{aligned}$$

where the transverse operators are defined as

$$\nabla_t \cdot \bar{A} = \frac{\partial A_x}{\partial x} + \frac{\partial A_y}{\partial y} \quad \nabla_t \Psi = \hat{x} \frac{\partial \Psi}{\partial x} + \hat{y} \frac{\partial \Psi}{\partial y}$$

By applying the two-dimensional Fourier transform of Equation (10.127) to the above equations and eliminating the z -components of the fields, show that the transformed equations can be expressed as

$$\begin{aligned} -\frac{\partial \tilde{E}_x}{\partial z} - \frac{j}{\omega\epsilon}(k^2 - k_x^2)\tilde{H}_y - \frac{jk_xk_y}{\omega\epsilon}\tilde{H}_x &= \tilde{K}_y + \frac{k_x}{\omega\epsilon}\tilde{J}_z \\ -\frac{\partial \tilde{E}_y}{\partial z} + \frac{j}{\omega\epsilon}(k^2 - k_y^2)\tilde{H}_x + \frac{jk_xk_y}{\omega\epsilon}\tilde{H}_y &= -\tilde{K}_x + \frac{k_y}{\omega\epsilon}\tilde{J}_z \\ -\frac{\partial \tilde{H}_x}{\partial z} + \frac{j}{\omega\mu}(k^2 - k_x^2)\tilde{E}_y + \frac{jk_xk_y}{\omega\mu}\tilde{E}_x &= -\tilde{J}_y + \frac{k_x}{\omega\mu}\tilde{K}_z \\ -\frac{\partial \tilde{H}_y}{\partial z} - \frac{j}{\omega\mu}(k^2 - k_y^2)\tilde{E}_x - \frac{jk_xk_y}{\omega\mu}\tilde{E}_y &= \tilde{J}_x + \frac{k_y}{\omega\mu}\tilde{K}_z \end{aligned}$$

where $k^2 = \omega^2\mu\epsilon$. These equations are functions of the variable z and the parameters k_x and k_y , and are similar in form to coupled transmission line equations.

- P10.15** Use the transmission line analogy developed in Section 10.10 to derive the Green's function for the electric field produced by an x -directed point source on the surface of a dielectric slab of thickness d . Then, use the Green's function to extend the conducting patch FSS formulation to the case of p.e.c. patches located on the surface of a dielectric slab. First provide the integral equation in a form similar to (10.151) and (10.152), with the appropriate Green's functions expressed in terms of inverse Fourier transform integrals. Then, introduce basis and testing functions $B(x, y)$ and $T(x, y)$ and combine the Poisson sum transformation with the convolution operation to obtain the matrix entries in the form of a double summation over the transforms \tilde{B} and \tilde{T} .